Probing the weak-boson sector in $Z\gamma$ production at hadron colliders

U. Baur
Physics Department, Florida State University, Tallahassee, Florida 32306

E. L. Berger
CERN, Geneva, Switzerland
*and High Energy Physics Division, Argonne National Laboratory, Argonne, Illinois 60439**

(Received 5 November 1992)

A detailed analysis of $Z\gamma$ production at hadron colliders is presented for general $ZZ\gamma$ and $Z\gamma\gamma$ couplings. Deviations from the standard model gauge theory structure can be parametrized in terms of four $ZZ\gamma$ and four $Z\gamma\gamma$ form factors. The high-energy behavior of these form factors is severely restricted by unitarity. Prospects for testing the self-interactions of Z bosons and photons at the Fermilab Tevatron, the CERN Large Hadron Collider and the Superconducting Super Collider are explored. Sensitivity limits for anomalous $ZZ\gamma$ and $Z\gamma\gamma$ couplings are derived and compared to bounds from low-energy data and e^+e^- collider experiments.

PACS number(s): 13.85.Qk, 12.15.Cc, 13.38.+c

I. INTRODUCTION

Experiments at the Fermilab Tevatron $p\bar{p}$ collider are expected to collect data corresponding to an integrated luminosity of approximately 100 pb^{-1} in the 1992–1993 run, an increase of more than one order of magnitude in statistics over the data sample presently available. The significant increase in integrated luminosity will make it possible to probe previously untested sectors of the standard model (SM) of electroweak interactions, such as the vector-boson self-interactions. Within the SM, at the tree level, these self-interactions are completely fixed by the $SU(2)\times U(1)$ gauge theory structure of the model. Their observation is thus a crucial test of the model. Recently, the UA2 Collaboration [1] reported the first direct measurement of the $WW\gamma$ vertex in the reaction $p\bar{p}\rightarrow e^{\pm}\nu\gamma X$. Within rather large errors the UA2 result is consistent with SM expectations. More precise information can soon be expected from $W^{\pm}\gamma$ production in the ongoing Tevatron run [2].

In addition to significantly improved bounds on the structure of the $WW\gamma$ vertex, the new Tevatron data will also offer the possibility to search for evidence of nonzero $ZZ\gamma$ and $Z\gamma\gamma$ couplings in $Z\gamma$ production. All $ZZ\gamma$ and $Z\gamma\gamma$ couplings vanish in the SM at the tree level, and the rates for $W^{\pm}\gamma$ and $Z\gamma$ production are quite similar [3]. In this paper we study the capabilities of future hadron collider experiments to probe the $ZZ\gamma$ and $Z\gamma\gamma$ vertices via $Z\gamma$ production. In the past, the reaction $p\bar{p}\rightarrow Z\gamma$ has usually been considered for a restricted set of anomalous couplings only [4,5]. We go a step further and use the most general $Z\gamma V, V=\gamma,Z$, vertex which is accessible in the annihilation process $q\bar{q}\rightarrow Z\gamma$ of effectively massless quarks. Four different anomalous couplings are allowed by electromagnetic gauge invariance and Lorentz invariance [6]. Their properties are discussed in Sec. II, where we also derive unitarity bounds for the form factors associated with the $ZZ\gamma$ and $Z\gamma\gamma$ vertices. We assume the SM to be valid apart from anomalies in the $ZZ\gamma$ and $Z\gamma\gamma$ vertices. In particular, we assume the couplings of W and Z bosons to quarks and leptons to be given by the SM and that there are no nonstandard couplings of the $Z\gamma$ pair to two gluons [7].

Our analysis is based on the calculation of helicity amplitudes for the complete processes

$$q\bar{q}\rightarrow Z\gamma\rightarrow l^+l^-\gamma \tag{1.1}$$

and

$$q\bar{q}\rightarrow Z\gamma\rightarrow \bar{\nu}\nu\gamma\ , \tag{1.2}$$

where $l=e,\mu$. In case of the $l^+l^-\gamma$ final state, timelike virtual photon and radiative Z decay diagrams also contribute. Together with effects of the finite Z width, these are included fully in our calculation. In Sec. III we discuss the signatures of anomalous $ZZ\gamma$ and $Z\gamma\gamma$ couplings in $p\bar{p}\rightarrow l^+l^-\gamma$ and $p\bar{p}\rightarrow\bar{\nu}\nu\gamma$ at the Tevatron, taking into account the form-factor behavior of the anomalous couplings. The $l^+l^-\gamma$ invariant mass, the photon transverse momentum, and the $\cos\Theta_l^*$ distributions are sensitive indicators of anomalous couplings. Here Θ_l^* is the polar angle in the l^+l^- rest frame with respect to the l^+l^- direction in the $ll\gamma$ rest frame. Cuts are described which select a region in phase space particularly sensitive to anomalous couplings. In Sec. III we also consider the most important backgrounds to (1.1) and (1.2). The sensitivity of experiments at the CERN Large Hadron Collider (LHC) and Superconducting Super Collider (SSC) to nongauge theory $Z\gamma V$ vertices is discussed in Sec. IV. In Sec. V we compare the limits on anomalous $ZZ\gamma$ and $Z\gamma\gamma$ couplings expected from future hadron collider experiments with low-energy bounds, and with the sensitivity from present and future e^+e^- collider experiments. In Sec. V we also present our conclusions.

*Permanent address.

II. $ZZ\gamma$ AND $Z\gamma\gamma$ COUPLINGS

At the parton level, the reaction $p\bar{p}\to l^+l^-\gamma$ proceeds via the Feynman graphs shown in Figs. 1 and 2. Figure 1 displays the full set of SM diagrams, whereas the contributions from anomalous $ZZ\gamma$ and $Z\gamma\gamma$ couplings are shown in Fig. 2. For $p\bar{p}\to\bar{\nu}\nu\gamma$, only the timelike virtual Z diagrams of Figs. 1(a) and 1(b) and Fig. 2(a) contribute. In both processes the timelike virtual photon and/or Z boson couples to essentially massless fermions, which ensures that effectively $\partial_\mu V^\mu=0$, $V=\gamma,Z$. This together with gauge invariance of the on-shell photon restricts the tensor structure of the $Z\gamma V$ vertex sufficiently to allow just four free parameters. The most general anomalous $Z\gamma Z$ vertex function (see Fig. 3 for notation) is given by [6]

$$\Gamma^{\alpha\beta\mu}_{Z\gamma Z}(q_1,q_2,P)=\frac{P^2-q_1^2}{m_Z^2}\left[h_1^Z(q_2^\mu g^{\alpha\beta}-q_2^\alpha g^{\mu\beta})+\frac{h_2^Z}{m_Z^2}P^\alpha[(P\cdot q_2)g^{\mu\beta}-q_2^\mu P^\beta]+h_3^Z\epsilon^{\mu\alpha\beta\rho}q_{2\rho}+\frac{h_4^Z}{m_Z^2}P^\alpha\epsilon^{\mu\beta\rho\sigma}P_\rho q_{2\sigma}\right], \quad (2.1)$$

where m_Z is the Z-boson mass. The most general $Z\gamma\gamma$ vertex function can be obtained from Eq. (2.1) by the following replacements:

$$\frac{P^2-q_1^2}{m_Z^2}\to\frac{P^2}{m_Z^2} \quad \text{and} \quad h_i^Z\to h_i^\gamma, \quad i=1,\ldots,4 . \quad (2.2)$$

Terms proportional to P^μ and q_1^α have been omitted in Eq. (2.1) since they do not contribute to the cross section. Without loss of generality we have chosen the overall $ZZ\gamma$ and $Z\gamma\gamma$ coupling constant to be

$$g_{ZZ\gamma}=g_{Z\gamma\gamma}=e , \quad (2.3)$$

where e is the charge of the proton. The overall factor $(P^2-q_1^2)$ in Eq. (2.1) is a result of Bose symmetry, whereas the factor P^2 in the $Z\gamma\gamma$ vertex function originates from electromagnetic gauge invariance. As a result the $Z\gamma\gamma$ vertex function vanishes identically if both photons are on shell [8].

The form factors h_i^V are dimensionless functions of q_1^2, q_2^2, and P^2. All couplings are C odd; h_1^V and h_2^V violate CP. Combinations of h_3^V (h_1^V) and h_4^V (h_2^V) correspond to the electric (magnetic) dipole and magnetic (electric) quadrupole transition moment. h_2^V and h_4^V receive only contributions from operators of dimension ≥ 8. Within the SM, at tree level, all couplings h_i^V vanish. At the one-loop level, only the CP-conserving couplings h_3^V and h_4^V are nonzero. For h_3^Z, for example, one finds [9]

$$2.2\times10^{-4}\leq h_3^Z\leq 2.5\times10^{-4} \quad (2.4)$$

for a top-quark mass m_t in the range between 100 and 200 GeV.

In Eq. (2.1), without loss of generality, we have chosen the Z boson mass m_Z as the energy scale in the denominator of the overall factor and the terms proportional to $h_{2,4}^V$. For a different mass scale M all subsequent results can be obtained by scaling $h_{1,3}^V$ ($h_{2,4}^V$) by a factor M^2/m_Z^2 (M^4/m_Z^4).

Tree-level unitarity restricts the $ZZ\gamma$ and $Z\gamma\gamma$ couplings uniquely to their SM values at asymptotically high energies [10]. This implies that the $Z\gamma V$ couplings h_i^V have to be described by form factors $h_i^V(q_1^2,q_2^2,P^2)$ which vanish when q_1^2, q_2^2, or P^2 becomes large. In $Z\gamma$ production $q_2^2=0$ and $q_1^2\approx m_Z^2$ even when finite Z width effects are taken into account. However, large values of $P^2=\hat{s}$ will be probed in future hadron collider experiments, and the $\hat{s}$ dependence has to be included in order to avoid unphysical results that would violate unitarity.

The values $h_{i0}^V=h_i^V(m_Z^2,0,0)$ of the form factors at low energy (at $\hat{s}=0$) are constrained by partial-wave unitarity of the inelastic vector-boson pair production amplitude in fermion antifermion annihilation at arbitrary center-of-mass energies. Since the couplings h_i^V do not contribute to $f\bar{f}\to ZZ$ [6], it is sufficient to consider partial-wave unitarity for $f\bar{f}\to Z\gamma$ only. In deriving unitarity limits

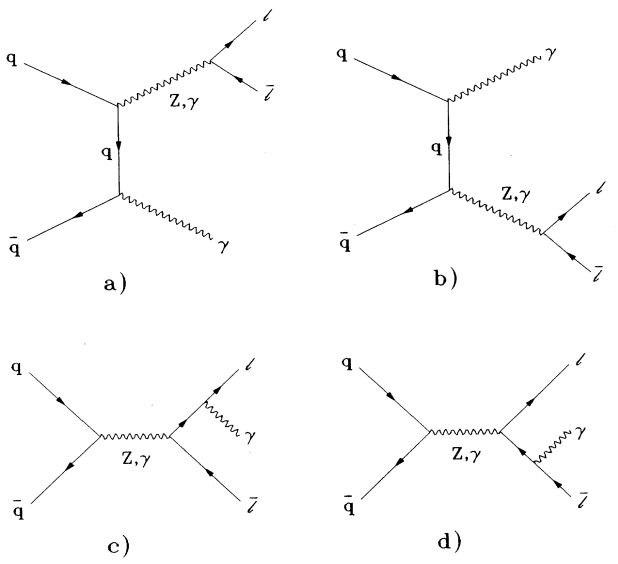

FIG. 1. Feynman graphs for the tree-level processes contributing to $p\bar{p}\to l^+l^-\gamma$ in the SM.

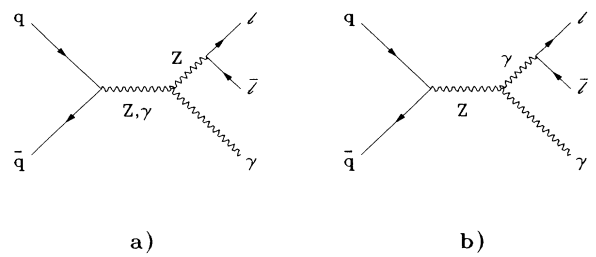

FIG. 2. Contributions of $ZZ\gamma$ and $Z\gamma\gamma$ diagrams to $q\bar{q}\to l^+l^-\gamma$.

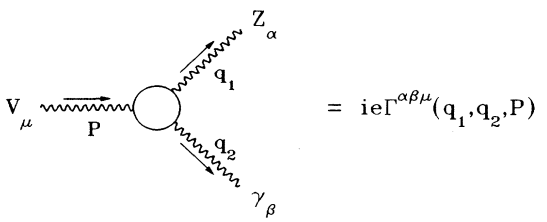

FIG. 3. Feynman rule for the general $Z\gamma V, V=Z,\gamma$ vertex. The vertex function Γ is given in Eq. (2.1). e is the charge of the proton.

for the h_{i0}^V's, we follow the strategy employed in Ref. [11]. The contribution of the $Z\gamma V$ diagram to the

$$f(\sigma)\bar{f}(\bar{\sigma})\to Z(\lambda_Z)\gamma(\lambda_\gamma)$$

helicity amplitudes can be written as

$$\Delta\mathcal{M}^V(\sigma\bar{\sigma},\lambda_Z\lambda_\gamma) = -\sqrt{2}e^2 g_{2\sigma}^{Vf\bar{f}}\frac{\hat{s}}{\hat{s}-m_V^2}\left[1-\frac{m_Z^2}{\hat{s}}\right]\delta_{\sigma,-\bar{\sigma}}A^V_{\lambda_Z\lambda_\gamma} \times d^1_{\sigma-\bar{\sigma},\lambda_Z-\lambda_\gamma}(\Theta)\ , \tag{2.5}$$

where $\sigma,\bar{\sigma}$ and λ_Z,λ_γ denote the helicities of the particles involved, and $g_{2\sigma}^{Vf\bar{f}}$ is the $Vf\bar{f}$ SM coupling constant. The dependence on the center-of-mass scattering angle Θ is given by the conventional d functions [12]. All terms involving the anomalous $Z\gamma V$ couplings are absorbed in the reduced amplitudes $A^V_{\lambda_Z\lambda_\gamma}$, which we have calculated for the vertex function (2.1) using the helicity techniques of Ref. [13].

Partial-wave unitarity then leads to the following bounds on the reduced amplitudes in the limit $\hat{s}\gg m_Z^2$:

$$\left[\sum_{\lambda_Z\lambda_\gamma}|A^Z_{\lambda_Z\lambda_\gamma}|^2\right]^{1/2}\le\frac{1}{\alpha}\left[\frac{3}{10}\right]^{1/2}4\sin\theta_W\cos\theta_W \tag{2.6}$$

and

$$\left[\sum_{\lambda_Z\lambda_\gamma}|A^\gamma_{\lambda_Z\lambda_\gamma}|^2\right]^{1/2} \le\frac{1}{\alpha}[\tfrac{3}{5}(3-6\sin^2\theta_W+8\sin^4\theta_W)]^{1/2}\ , \tag{2.7}$$

where $\alpha=\frac{1}{128}$ is the electromagnetic coupling constant, and θ_W the Weinberg angle. To transform the inequalities (2.6) and (2.7) into bounds on the h_{i0}^V's, assumptions on the form-factor behavior have to be made. For deviations of the $Z\gamma V$ couplings from zero which are produced by some novel interactions operative at a scale Λ, one should expect that the form factors stay essentially constant for $\hat{s}\ll\Lambda^2$ and start decreasing only when the scale Λ is reached or surpassed, very much like the well-known nucleon form factors. With this example in mind, we shall use generalized dipole form factors of the form

$$h_i^V(m_Z^2,0,\hat{s})=\frac{h_{i0}^V}{(1+\hat{s}/\Lambda^2)^n}\ . \tag{2.8}$$

Assuming that only one anomalous coupling is nonzero at a time, one finds, for $\Lambda\gg m_Z$,

$$|h_{10}^Z|,|h_{30}^Z|<\frac{(\frac{2}{3}n)^n}{(\frac{2}{3}n-1)^{n-3/2}}\frac{0.126\ \text{TeV}^3}{\Lambda^3}\ ,$$
$$|h_{20}^Z|,|h_{40}^Z|<\frac{(\frac{2}{5}n)^n}{(\frac{2}{5}n-1)^{n-5/2}}\frac{2.1\times10^{-3}\ \text{TeV}^5}{\Lambda^5}\ , \tag{2.9}$$

and

$$|h_{10}^\gamma|,|h_{30}^\gamma|<\frac{(\frac{2}{3}n)^n}{(\frac{2}{3}n-1)^{n-3/2}}\frac{0.151\ \text{TeV}^3}{\Lambda^3}\ ,$$
$$|h_{20}^\gamma|,|h_{40}^\gamma|<\frac{(\frac{2}{5}n)^n}{(\frac{2}{5}n-1)^{n-5/2}}\frac{2.5\times10^{-3}\ \text{TeV}^5}{\Lambda^5}\ . \tag{2.10}$$

The bounds listed in (2.9) and (2.10) have been computed with $m_Z=91.1$ GeV and $\sin^2\theta_W=0.23$. They are in agreement with those derived in Ref. [14].

Tree-level unitarity is satisfied throughout the entire $\hat{s}$ range when the limits of (2.9) and (2.10) are observed. For the more likely case that several anomalous couplings contribute, cancellations may occur and the bounds are weaker than those listed in Eqs. (2.9) and (2.10). From the n dependent factors in (2.9) and (2.10) one observes that $n>\frac{3}{2}$ for $h_{1,3}^V$, and $n>\frac{5}{2}$ for $h_{2,4}^V$ in order to satisfy unitarity. This is a direct consequence of the high-energy behavior of the anomalous contributions to the $Z\gamma$ helicity amplitudes, which grow like $(\sqrt{\hat{s}}/m_Z)^3$ for $h_{1,3}^V$, and $(\sqrt{\hat{s}}/m_Z)^5$ for $h_{2,4}^V$.

Inspection of the anomalous contributions to the helicity amplitudes also reveals that the dominant terms in the very-high-energy limit all originate from $\Delta\mathcal{M}^V(\sigma\bar{\sigma},0\pm)$. Anomalous $ZZ\gamma$ and $Z\gamma\gamma$ couplings therefore lead to an enhanced production of longitudinal Z bosons in the final state which can be detected in the angular distribution of the final-state charged leptons. We shall come back to this point in Sec. III B.

The vertex function (2.1), augmented by the form-factor ansatz (2.8), represents a self-consistent model of anomalous $ZZ\gamma$ and $Z\gamma\gamma$ interactions, as long as the bounds (2.9) and (2.10) are respected. This statement becomes transparent if one notes that the momentum dependence of the couplings h_i^V can also be viewed as an effect of higher-order loop corrections involving anomalous $ZZ\gamma$ or $Z\gamma\gamma$ interactions. These corrections effectively give rise to higher-dimensional operators, which can be summed and absorbed in the vertex function (2.1). As a result, the couplings h_i^V become momentum dependent form factors. All details of the underlying model are contained in the specific functional form of the form factor and its scale Λ.

The unitarity bounds shown in (2.9) and (2.10) depend strongly on the scale Λ. This strong dependence originates from the overall factors $(P^2-q_1^2)/m_Z^2$ and P^2/m_Z^2, respectively, which, in turn, are responsible for a factor $1/\Lambda^2$ in the unitarity limits. Unlike $W\gamma$ production, where form-factor effects do not play a crucial role, these Λ dependent effects cannot be ignored in $Z\gamma$ production at Tevatron energies. Unless stated otherwise, we shall assume that $n=3$ for $h_{1,3}^V$, and $n=4$ for $h_{2,4}^V$. These

choices guarantee that unitarity is preserved and that terms proportional to $h^V_{20,40}$ have the same high-energy behavior as those proportional to $h^V_{10,30}$. Furthermore, if exponents sufficiently above the minimum values of $\frac{3}{2}$ and $\frac{5}{2}$ are selected, one ensures that $Z\gamma$ production is suppressed at energies $\sqrt{\hat{s}} \gg \Lambda \gg m_Z$, where novel phenomena such as multiple weak boson, or resonance production, are expected to dominate.

III. SIGNATURES OF ANOMALOUS $ZZ\gamma$ AND $Z\gamma\gamma$ COUPLINGS AT THE TEVATRON

A. Preliminaries

We shall now discuss the signatures of anomalous couplings at the Tevatron. The signal consists of an isolated high transverse momentum (p_T) photon and a Z boson which may decay hadronically or leptonically. The hadronic Z decay modes will be difficult to observe due to the QCD $jj\gamma$ background [15]. In the following we therefore focus on the leptonic decay modes of the Z boson. If the Z decays into a e^+e^- or $\mu^+\mu^-$ pair (we neglect the τ decay mode), the signal is

$$p\bar{p} \to l^+l^-\gamma \ , \tag{3.1}$$

where $l = e, \mu$. The process (3.1) will be considered in detail in Sec. III B. In addition to the Feynman graphs for $Z\gamma$ production [Figs. 1(a), 1(b), and 2(a)], timelike virtual photon graphs and final-state bremsstrahlungs diagrams [Figs. 1(c), 1(d), and 2(b)] also contribute to this reaction. We incorporate their effects in our numerical simulations, together with the finite Z-boson width. Matrix elements are calculated using the helicity technique described in Ref. [13], and cross sections and dynamical distributions are evaluated using a parton level Monte Carlo program.

If the Z boson decays into a pair of neutrinos, the experimental signal is

$$p\bar{p} \to \gamma \not{p}_T \ , \tag{3.2}$$

with the missing transverse momentum $\not{p}_T$ resulting from the nonobservation of the neutrino pair. Only the diagrams of Figs. 1(a), 1(b), and 2(a) contribute to (3.2). This process will be investigated in Sec. III C. In Sec. III D we shall derive sensitivity limits for anomalous $ZZ\gamma$ and $Z\gamma\gamma$ couplings from Tevatron experiments.

In our calculations we simulate the finite acceptance of detectors by cuts imposed on observable particles in the final state. In this section, unless otherwise stated explicitly, we require a photon transverse momentum of $p_{T\gamma} > 10$ GeV, a charged lepton p_T of $p_{Tl} > 15$ GeV, and a charged lepton-photon separation in the pseudorapidity-azimuthal angle plane of

$$\Delta R_{l\gamma} = [(\Delta\Phi_{l\gamma})^2 + (\Delta\eta_{l\gamma})^2]^{1/2} > 0.7 \ . \tag{3.3}$$

We also impose a cut on the invariant mass of the charged lepton pair of $m_{ll} > 10$ GeV, and pseudorapidity cuts of $|\eta_\gamma| < 3$ and $|\eta_l| < 3.5$ on the photon and the charged leptons, respectively. Without finite m_{ll}, $p_{T\gamma}$, p_{Tl}, and $\Delta R_{l\gamma}$ cuts, the cross section for (3.1) would diverge, due to the various collinear and infrared singularities present at the order in which we are working.

The transverse momentum and pseudorapidity cuts listed above approximate the phase-space region covered by the Collider Detector at Fermilab (CDF) and D0 detector at the Tevatron [16,17]. The requirements on the charged leptons may appear to be somewhat loose, but relaxing the p_{Tl} and η_l cuts as much as possible may be advantageous in the search for anomalous $ZZ\gamma$ and $Z\gamma\gamma$ couplings. We shall discuss this point in more detail in Sec. III B.

Uncertainties in the energy measurements of the charged leptons and the photon are taken into account in our numerical simulations by Gaussian smearing of the particle momenta with standard deviation

$$\frac{\sigma}{E} = \begin{cases} 0.135/\sqrt{E_T} \oplus 0.02 & \text{for } |\eta| < 1.1 \ , \\ 0.28/\sqrt{E} \oplus 0.02 & \text{for } 1.1 < |\eta| < 2.4 \ , \\ 0.25/\sqrt{E} \oplus 0.02 & \text{for } 2.4 < |\eta| < 4.2 \ , \end{cases} \tag{3.4}$$

corresponding to the CDF detector resolution [16]. E (E_T) in Eq. (3.4) is the energy (transverse energy) of the particle, and the symbol $\oplus$ that the constant term is added in quadrature in the resolution. The only visible effect of the finite energy resolution in the figures presented below arises in regions of phase space where the cross section changes very rapidly, e.g., around the Z-boson peak. The resolution of the D0 detector [18] is better than that of the CDF detector. Smearing effects are therefore less pronounced if the D0 parametrization for σ/E is used. We shall assume in all our calculations below that leptons and photons can be detected with 100% efficiency in the phase-space region allowed by the cuts.

The SM parameters used in our calculations are $\alpha = \alpha(m_Z^2) = \frac{1}{128}$, $\alpha_s(m_Z^2) = 0.12$ [19], $m_Z = 91.1$ GeV, and $\sin^2\theta_W = 0.23$. For the parton distribution functions we used the updated leading order Duke-Owens (DO) set 1 (DO1.1) [20] with the scale Q^2 given by the parton center-of-mass squared, $\hat{s}$. We make no attempt to include the effects of next-to-leading-log (NLL) QCD corrections to $q\bar{q} \to Z\gamma$, or the contributions from gluon fusion, $gg \to Z\gamma$, into our calculations. NLL QCD corrections to $q\bar{q} \to Z\gamma$ have been calculated recently in the framework of the SM for a stable, on-shell Z boson [21]. At Tevatron energies they increase the cross section by typically 20–30%. For $p_{T\gamma} > 10$ GeV and $|\eta_\gamma| < 3$, gluon fusion contributes less than 0.2% to the total $Z\gamma$ cross section at $\sqrt{s} = 1.8$ TeV [22], and thus it can be neglected at current hadron collider energies.

The Feynman diagrams shown in Fig. 1 can be divided into four gauge-invariant subsets. Timelike virtual photon and Z-boson graphs are separately gauge invariant. Furthermore, the diagrams of Figs. 1(a), 1(b) and Figs. 1(c), 1(d) form gauge-invariant subsets. This separation greatly facilitates comparing our results in the SM case with results published in the literature. For example, our squared matrix element for final-state bremsstrahlung [Figs. 1(c) and 1(d)] agrees numerically completely with that of Ref. [23]. The two diagrams of Fig. 2 are also individually gauge invariant. It is therefore sensible to

display the contribution induced by nonzero $ZZ\gamma$ or $Z\gamma\gamma$ couplings separately from the SM and the total result. In order to study the effects of anomalous couplings on various distributions, we shall make use of this possibility in some of the figures below.

B. $p\bar{p} \to l^+ l^- \gamma$

In the $q\bar{q} \to Z\gamma$ subprocess the effects of anomalous $ZZ\gamma$ and $Z\gamma\gamma$ couplings are enhanced at large energies. If the Z boson decays into a pair of charged leptons, a typical signal for nonstandard couplings will be a broad increase in the invariant mass distribution $d\sigma/dm_{ll\gamma}$ of the final state $l^+ l^- \gamma$ system at large values of $m_{ll\gamma}$. This result is demonstrated in Fig. 4, which shows the $ll\gamma$ invariant mass distribution for the cuts described in Sec. III A. Here, and in all subsequent figures of this subsection, we shall always sum over electron and muon final states. The solid line gives the result of the full set of SM Feynman diagrams. Because of the finite detector resolution effects, the Z-boson resonance is broadened, and the peak cross section is significantly reduced. The sharp dip at $m_{ll\gamma} \approx 100$ GeV is due to the $p_{T\gamma} > 10$ GeV cut. In the vicinity of the Z peak, the cross section is completely dominated by radiative Z decays (dashed line), whereas at large invariant masses $Z\gamma$ production (dotted curve) prevails. Timelike virtual photon diagrams dominate only below the Z resonance, accounting for the difference below the resonance between the solid and dashed curves. At large values of $m_{ll\gamma}$ they contribute about 20–30 % to the cross section for the set of cuts chosen. Because of the finite p_T and separation cuts imposed, the cross section drops rapidly below an invariant mass of 60 GeV.

The dash dotted line in Fig. 4 shows the contribution of the diagram shown in Fig. 2(a) to the $ll\gamma$ invariant mass distribution for $h_{30}^Z = 2$ and a form-factor scale $\Lambda = 0.75$ TeV. This rather large value of h_{30}^Z, which is just below the unitarity limit, Eq. (2.9), has been chosen to demonstrate the increase in cross section with $m_{ll\gamma}$. At large invariant masses the anomalous contributions dominate, whereas they are approximately two orders of magnitude smaller than the SM terms in the region around the Z peak. The strong dip present in the dash dotted curve at $m_{ll\gamma} \approx 100$ GeV originates from the interplay between the Breit-Wigner form of the s-channel Z boson and the growth of the nonstandard amplitude, proportional to $(\sqrt{\hat{s}}/m_Z)^3$ at large energies.

The information obtained from the $m_{ll\gamma}$ distribution is supplemented by that from the invariant mass spectrum of the charged lepton pair, $d\sigma/dm_{ll}$, which is shown in Fig. 5. For the cuts chosen, the peak of the final state Z boson is clearly visible in the full SM distribution (solid line). The dip at $m_{ll} \approx 80$ GeV originates from the finite p_T cut on the photon. In the region 20 GeV $\leq m_{ll} \leq 80$ GeV, the contribution from radiative Z decays (dashed line) dominates. Because of the infrared singularity, the lepton pair invariant mass distribution in $Z \to l^+ l^- \gamma$ peaks close to the upper kinematical limit of m_{ll}. Timelike virtual photon diagrams contribute primarily at low invariant masses, due to the $1/m_{ll}^2$ mass singularity in the squared matrix element of the timelike virtual γ graphs, and above the Z resonance peak. Nonstandard couplings affect primarily the Z peak region, as demonstrated by the dash dotted line for $h_{30}^Z = 2$ and $\Lambda = 0.75$ TeV.

Anomalous couplings contribute only via the s-channel Z and timelike virtual photon graphs of Fig. 2, and hence only to the $J = 1$ partial wave when fermion masses are neglected. Nonstandard contributions are therefore al-

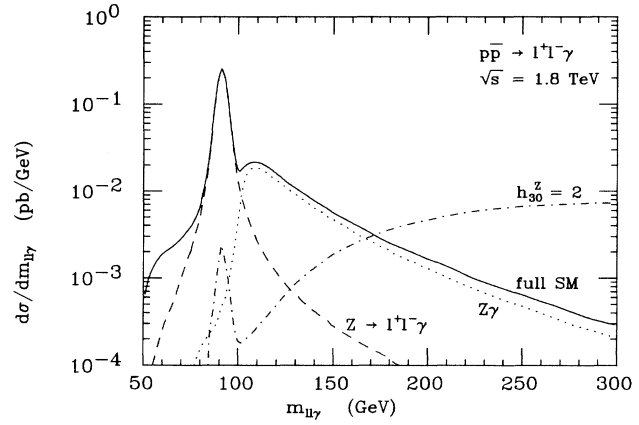

FIG. 4. Invariant mass distribution of the $ll\gamma$ system in $p\bar{p} \to l^+ l^- \gamma$ at the Tevatron. The solid curve shows the result of the full SM set of tree-level diagrams. The dashed line displays the portion from radiative Z decays [final-state bremsstrahlung, Figs. 1(c) and 1(d)], whereas the dotted line gives the result of the SM $q\bar{q} \to Z\gamma, Z \to l^+ l^-$ diagrams [Figs. 1(a) and 1(b)]. The dash-dotted curve, finally, shows the invariant mass distribution obtained from the diagram of Fig. 2(a) for $h_{30}^Z = 2$ and $\Lambda = 0.75$ TeV. The cuts used are detailed in Sec. III A.

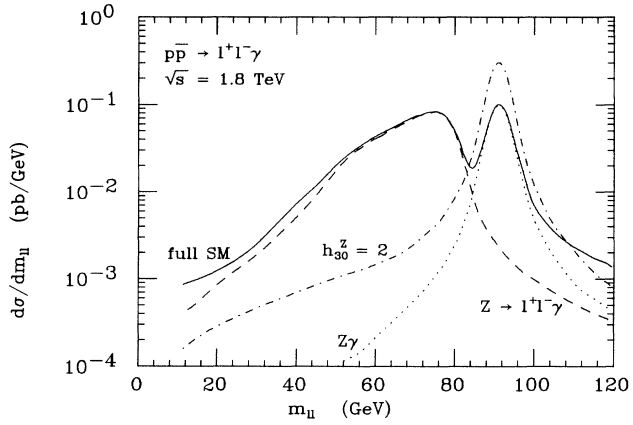

FIG. 5. Charged lepton pair invariant mass distribution for the process $p\bar{p} \to l^+ l^- \gamma$ at the Tevatron. The solid curve shows the result of the full SM set of tree-level diagrams. The dashed line displays the portion from radiative Z decays [final-state bremsstrahlung, Figs. 1(c) and 1(d)], whereas the dotted line gives the result of the SM $q\bar{q} \to Z\gamma, Z \to l^+ l^-$ diagrams [Figs. 1(a) and 1(b)]. The dash-dotted curve, finally, shows the invariant mass distribution obtained from the diagram of Fig. 2(a) for $h_{30}^Z = 2$ and $\Lambda = 0.75$ TeV. The cuts used are described in Sec. III A.

most isotropic in the center-of-mass frame and lead to a sharp peak in the charged lepton-photon separation at $\Delta R_{l\gamma} \approx \pi$. In Fig. 6 we compare the $\Delta R_{l^+\gamma}$ distribution resulting from the diagram of Fig. 2(a) for $h_{30}^Z = 2$ and $\Lambda = 0.75$ TeV (dash dotted line) with the SM charged lepton-photon separation spectrum (solid line) for the cuts described in Sec. III A. The $\Delta R_{l\gamma} > 0.7$ cut is seen to have almost no effect on the signal from anomalous couplings. In the SM, the $\Delta R_{l^+\gamma}$ distribution exhibits a sharp rise at small separation, and a pronounced peak at larger values of $\Delta R_{l^+\gamma}$. Both structures arise from the collinear singularities present for final-state bremsstrahlung (dashed curve). The peaking of the cross section at small lepton-photon separation reflects the singularity which is present when the photon is radiated from the l^+ line. The maximum at larger values of $\Delta R_{l^+\gamma}$ originates from the collinear singularity for photon radiation from the l^- leg. At very large values of $\Delta R_{l^+\gamma}$, the SM distribution is dominated by the contribution from $q\bar{q} \to Z\gamma$, $Z \to l^+ l^-$ (dotted line), which exhibits a rather flat maximum at $\Delta R_{l^+\gamma} \approx \pi$. The distribution of the $l^-\gamma$ separation is identical to $d\sigma/d\Delta R_{l^+\gamma}$.

The large separation induced by the anomalous couplings suggests that the final-state photon and Z boson are produced primarily back to back for anomalous $ZZ\gamma$ and $Z\gamma\gamma$ couplings, and with large average transverse momentum. This feature is visible in Fig. 7, where we show the $p_{T\gamma}$ spectrum for the cuts discussed in Sec. III A. Anomalous couplings lead to a very broad photon transverse momentum distribution, as exemplified for $h_{30}^Z = 2$ and $\Lambda = 0.75$ TeV (dash dotted curve). The SM $p_{T\gamma}$ spectrum, on the other hand, falls steeply, and is

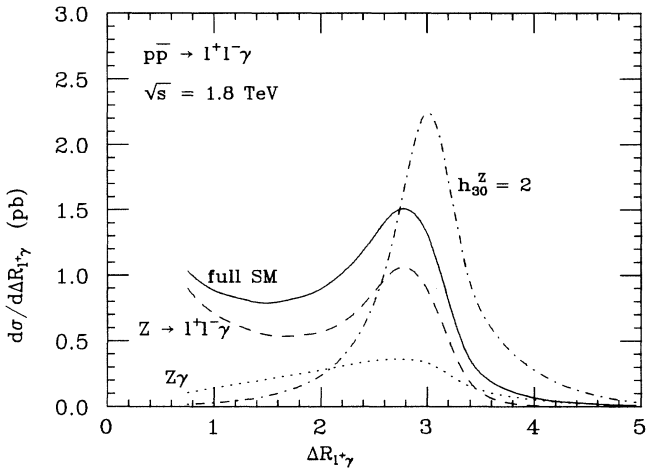

FIG. 6. Distribution of the $l^+\gamma$ separation, $d\sigma/d\Delta R_{l^+\gamma}$, in $p\bar{p} \to l^+ l^- \gamma$ at the Tevatron. The solid curve shows the result of the full SM set of tree-level diagrams. The dashed line displays the portion from radiative Z decays [final-state bremsstrahlung, Figs. 1(c) and 1(d)], whereas the dotted line gives the result of the SM $q\bar{q} \to Z\gamma, Z \to l^+ l^-$ diagrams [Figs. 1(a) and 1(b)]. The dash-dotted curve, finally, shows the $\Delta R_{l^+\gamma}$ distribution obtained from the diagram of Fig. 2(a) for $h_{30}^Z = 2$ and $\Lambda = 0.75$ TeV. The cuts used are detailed in Sec. III A.

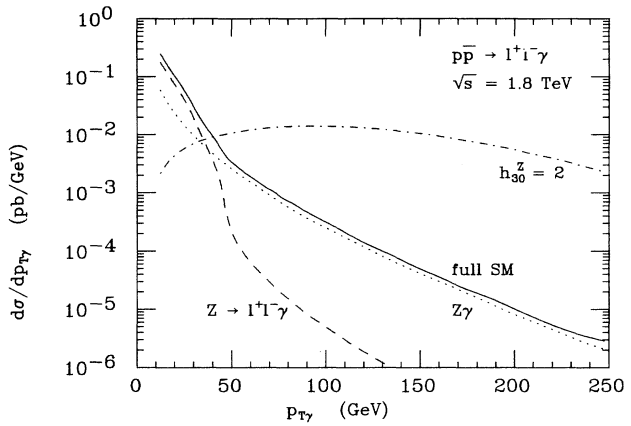

FIG. 7. Photon transverse momentum distribution in $p\bar{p} \to l^+ l^- \gamma$ at the Tevatron. The solid curve shows the result of the full SM set of tree-level diagrams. The dashed line displays the portion from radiative Z decays [final-state bremsstrahlung, Figs. 1(c) and 1(d)], whereas the dotted line gives the result of the SM $q\bar{q} \to Z\gamma, Z \to l^+ l^-$ diagrams [Figs. 1(a) and 1(b)]. The dash-dotted curve, finally, shows the $p_{T\gamma}$ distribution obtained from the diagram of Fig. 2(a) for $h_{30}^Z = 2$ and $\Lambda = 0.75$ TeV. The cuts used are described in Sec. III A.

dominated at low (high) transverse momenta by the $Z \to l^+ l^- \gamma$ ($q\bar{q} \to Z\gamma, Z \to l^+ l^-$) contribution. It is clear from Fig. 7 that the transverse momentum cut of $p_{T\gamma} > 10$ GeV will not affect the observability of anomalies in the $ZZ\gamma$ and $Z\gamma\gamma$ vertices.

In Figs. 4–7 we have shown results only for the anomalous $ZZ\gamma$ coupling h_3^Z. Qualitatively similar results can be obtained for other $ZZ\gamma$ as well as $Z\gamma\gamma$ couplings. For nonstandard $Z\gamma\gamma$ couplings, the diagram shown in Fig. 2(a) dominates at large invariant masses. In the vicinity of the Z peak and for $m_{ll} < 60$ GeV, on the other hand, the graph of Fig. 2(b) accounts for the largest part of the anomalous contribution to the cross section.

The results shown so far suggest that large invariant mass cuts of

$$m_{ll\gamma} > 100 \text{ GeV}, \quad m_{ll} > 50 \text{ GeV}, \tag{3.5}$$

would select a region in phase-space particularly sensitive to nonstandard $ZZ\gamma$ and $Z\gamma\gamma$ vertices. We shall impose these cuts, in addition to those described in Sec. III A, for the following more detailed investigation. In the SM the subprocess $q\bar{q} \to Z\gamma, Z \to l^+ l^-$ is the dominant contribution to $q\bar{q} \to l^+ l^- \gamma$ in the selected region of phase space.

Effects of nongauge theory trilinear $ZZ\gamma$ and $Z\gamma\gamma$ couplings are expected to be almost isotropic in the center-of-mass frame, and thus should populate primarily the central region in photon rapidity. Figure 8 demonstrates that this is indeed the case. With exception of the photon rapidity cut, the cuts applied are those described in Sec. III A and Eq. (3.5). The dashed line shows the photon rapidity distribution for $h_{30}^Z = 1$, $\Lambda = 0.75$ TeV, while the solid line gives the SM result. The full set of Feynman graphs shown in Figs. 1 and 2 was used to obtain the dashed curve. Figure 8 also shows that the

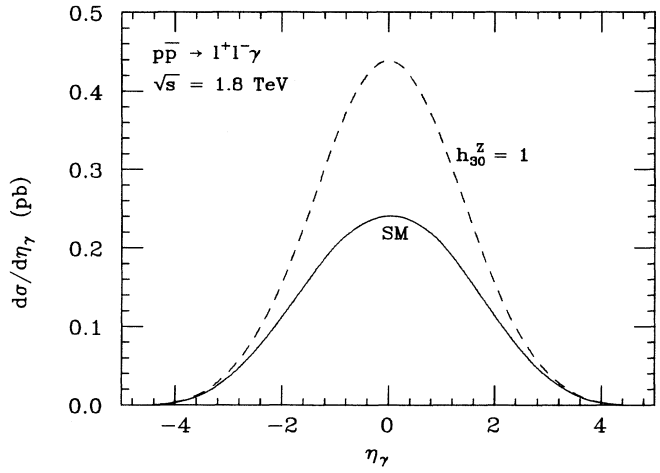

FIG. 8. Photon rapidity distribution in $p\bar{p} \to l^+l^-\gamma$ at the Tevatron. The solid curve shows the result of the full SM set of tree-level diagrams. The dashed line shows $d\sigma/d\eta_\gamma$ for $h_{30}^Z = 1$, $\Lambda = 0.75$ TeV. The cuts used are described in the text.

effects of the anomalous couplings extend out to $|\eta_\gamma| \approx 3$. For a cut more stringent than $|\eta_\gamma| < 3$ a significant part of the signal would be lost.

As mentioned in Sec. II, anomalous $ZZ\gamma$ and $Z\gamma\gamma$ couplings lead to primarily longitudinally polarized Z bosons in the final state. The polarization of the Z boson manifests itself in the angular distribution $d\sigma/d\cos\Theta_{l^\pm}^*$ of the charged leptons, which thus acts as an effective spin analyzer of the Z boson. Here Θ_l^* is the polar angle in the l^+l^- rest frame with respect to the l^+l^- direction in the $ll\gamma$ rest frame. Since the Z-boson coupling to charged leptons is almost purely axial vector, transverse Z bosons produce a $(1+\cos^2\Theta_l^*)$ distribution, while the angular distribution for longitudinal Z's is proportional to $\sin^2\Theta_l^*$.

Keeping this in mind, one recognizes from Fig. 9(a) that the angular distribution of the final-state charged leptons in $p\bar{p} \to l^+l^-\gamma$ provides an excellent SM test. The $\cos\Theta_{l^-}^*$ distribution clearly exhibits the dominance of transverse Z bosons in the SM (solid line). The rapid drop of the cross section for $|\cos\Theta_{l^-}^*| > 0.9$ originates from the finite transverse momentum and rapidity cuts on the charged leptons (see below). In the presence of anomalous couplings, the minimum at $\cos\Theta_{l^-}^* = 0$ is partially filled in. This point is illustrated by the dashed line which shows $d\sigma/d\cos\Theta_{l^-}^*$ for $h_{30}^Z = 1$, $\Lambda = 0.75$ TeV. The dotted line, finally, displays the contribution from the nonstandard coupling alone, exhibiting the form of an almost perfect $\sin^2\Theta_{l^-}^*$ curve. The charged lepton acceptance cuts are seen to reduce the signal of new physics only insignificantly. The l^+ angular distribution is identical to $d\sigma/d\cos\Theta_{l^-}^*$ in its form.

The apparent shape difference between the $\cos\Theta_{l^-}^*$ distribution in the presence of anomalous couplings and for the SM depends, however, to a large extent on the p_{Tl} and η_l cut imposed. This dependence is illustrated in Fig. 9(b), where we compare the SM charged lepton angular distribution for various lepton transverse momentum and pseudorapidity cuts. All other cuts are as described before. It is evident that the charged lepton angular distribution in the SM is quite sensitive to the cuts imposed. Increasing the p_{Tl} cut to 20 GeV, for example, starts to cut away the "wings" (dashed line). For a more stringent rapidity cut of $|\eta_l| < 2$ the $\cos\Theta_{l^-}^*$ distribution shows almost no trace of the $(1+\cos^2\Theta_l^*)$ form (dotted line). Relaxing the p_T and rapidity cuts on the charged leptons as much as possible will therefore help to make the lepton angular distribution a useful tool in discriminating between the SM and anomalous $ZZ\gamma$ or $Z\gamma\gamma$ couplings. It is interesting to note that the shape is changed less if only one of the leptons is required to be

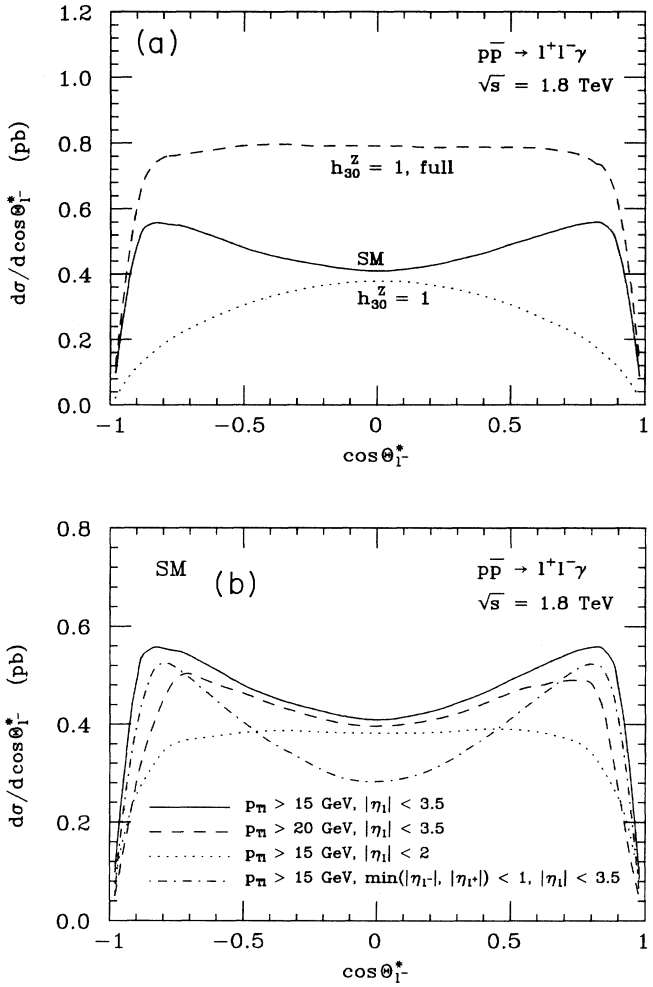

FIG. 9. Polar angle distribution of the charged lepton, l^-, in $p\bar{p} \to l^+l^-\gamma$ at the Tevatron. See the text for the definition of $\Theta_{l^-}^*$. (a) Comparison of $d\sigma/d\cos\Theta_{l^-}^*$ in the SM (solid curve) and for an anomalous $ZZ\gamma$ coupling of $h_{30}^Z = 1$, $\Lambda = 0.75$ TeV (dashed line). The dotted line shows the angular distribution for the anomalous diagram, Fig. 2(a), only. The cuts described in Sec. III A and Eq. (3.5) are imposed. (b) Dependence of $d\sigma/d\cos\Theta_{l^-}^*$ on the charged lepton transverse momentum and rapidity cuts in the SM. All other cuts are as in part (a) of the figure.

central. This point is illustrated by the dash-dotted curve, where we have required that one of the two leptons be in the range $|\eta_l| < 1$. For the CDF case, this condition must be satisfied for muon triggers.

So far, we have shown the effects of anomalous couplings for a single type of coupling h_3^Z and one form-factor scale Λ only. In Fig. 10 we investigate in more detail the influence of the form-factor behavior, as well as the effect of other anomalous couplings, on the $ll\gamma$ invariant mass distribution for the cuts of (3.5) and Sec. III A. In Fig. 10(a) we compare the SM mass spectrum with that of $h_{30}^Z = 1$, and $h_{40}^Z = 0.05$ for $\Lambda = 0.75$ TeV. Only one coupling at a time is chosen different from its zero SM value. Both coupling constants are approximately a factor 2 below the unitarity limit of Eq. (2.9). Since h_4^Z receives contributions only from operators with dimension ≥ 8, terms in the helicity amplitudes proportional to it grow like $(\sqrt{\hat{s}}/m_Z)^5$. Deviations originating from h_4^Z, therefore, start at higher invariant masses and rise much faster than contributions from couplings such as h_3^Z which correspond to dimension 6 operators.

For equal coupling strengths, the numerical results obtained for the $Z\gamma\gamma$ couplings h_3^γ and h_4^γ are about 20% below those obtained for h_3^Z and h_4^Z in the region where anomalous coupling effects dominate over the SM cross section. Results for the *CP*-violating couplings $h_{1,2}^V$, $V = Z, \gamma$ are virtually identical to those obtained for the same values of $h_{3,4}^V$. Whereas $h_{1,3}^V$ and $h_{2,4}^V$ can be distinguished from their different impact on the $l^+l^-\gamma$ invariant mass distribution, it will be more difficult to separate *CP*-conserving and *CP*-violating couplings, or $ZZ\gamma$ and $Z\gamma\gamma$ couplings at hadron colliders.

A potentially serious background to $p\bar{p} \to l^+l^-\gamma$ may arise from l^+l^-j production with the jet (j) misidentified as a photon. Such misidentifications originate primarily from jets hadronizing with a leading π^0, which carries away most of the jet energy. The probability $P_{\gamma/j}$ that a jet fakes a photon has so far not been determined in Tevatron experiments. In order to get an idea how severe the l^+l^-j background may be, we make use of the recent measurement of $P_{\gamma/j}$ in $p\bar{p} \to e^\pm \nu\gamma$ by UA2 [1]. It can be parametrized in the form

$$P_{\gamma/j}^{\mathrm{UA2}} = Ae^{-\beta p_{Tj}} \tag{3.6}$$

with $A = 0.039 \pm 0.0013$ and $\beta = 0.153 \pm 0.004$ GeV^{-1}. p_{Tj} in Eq. (3.6) denotes the jet transverse momentum. For large values of p_{Tj}, $P_{\gamma/j}^{\mathrm{UA2}}$ becomes extremely small. To remain on the safe side, we therefore introduce a cutoff of 1×10^{-4} for $P_{\gamma/j}$ and use

$$P_{\gamma/j} = \max(P_{\gamma/j}^{\mathrm{UA2}}, 1 \times 10^{-4}) \ . \tag{3.7}$$

The matrix elements for $q\bar{q} \to l^+l^-g$ and $qg \to l^+l^-q$, including timelike virtual photon diagrams, can be calculated with helicity techniques. The result of our numerical simulation is shown by the dash dotted line in Fig. 10(a). We conclude that, if $P_{\gamma/j}$ is less than a few percent at small p_T, and $\lesssim (10^{-4})$ at large transverse momenta, the l^+l^-j background does not severely limit the sensitivity of the $ll\gamma$ invariant mass distribution to anomalous couplings.

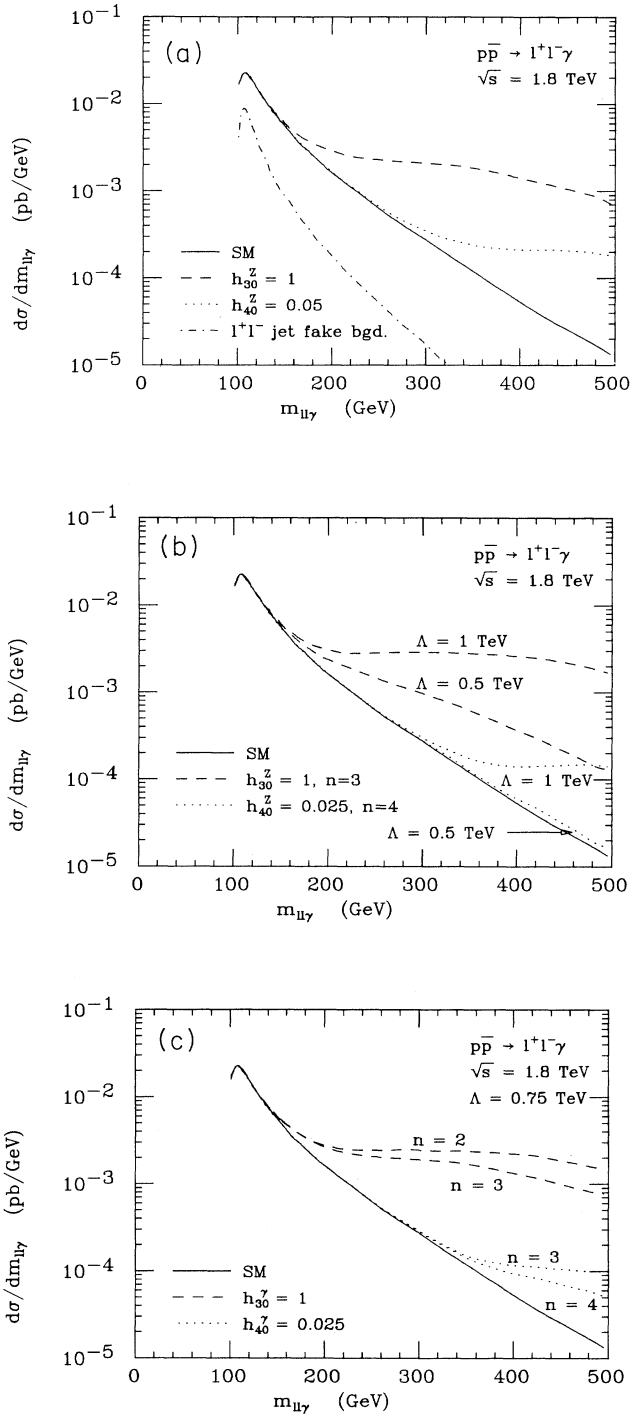

FIG. 10. Invariant mass distribution of the $ll\gamma$ system at the Tevatron for the cuts listed in Eq. (3.5) and Sec. III A. (a) $d\sigma/dm_{ll\gamma}$ for the SM (solid line) and two anomalous $ZZ\gamma$ couplings with $\Lambda = 0.75$ TeV. The dash dotted line represents the l^+l^-j background with the probability for a jet faking a photon given by Eqs. (3.6) and (3.7). (b) invariant mass spectrum for the SM (solid line) and two $ZZ\gamma$ couplings with two choices of the form-factor scale Λ. (c) $d\sigma/dm_{ll\gamma}$ for the SM (solid curve) and two $Z\gamma\gamma$ couplings with $\Lambda = 0.75$ TeV and two choices of the form-factor power n [see Eq. (2.8) for definition of n].

In Figs. 10(b) and 10(c) we investigate the dependence of the effects of anomalous $ZZ\gamma$ and $Z\gamma\gamma$ couplings on the scale and the power of the form factor Eq. (2.8). One observes that results depend significantly on the scale Λ chosen. For $\Lambda=1$ TeV the two couplings chosen in Fig. 10(b) are approximately at the unitarity limit. The power of the form factor in Fig. 10(b) was chosen to be $n=3$ ($n=4$) for h_3^Z (h_4^Z), as in all previous figures. As expected, the effects of anomalous couplings grow with increasing Λ. Similarly, a less drastic cutoff of $n=2$ ($n=3$) leads to additional events at large invariant masses, as shown in Fig. 10(c) for h_3^γ and h_4^γ with $\Lambda=0.75$ TeV.

C. $p\bar{p}\to\gamma\not{p}_T$

If the Z boson produced in $q\bar{q}\to Z\gamma$ decays into neutrinos, the signal consists of a high p_T photon accompanied by a large amount of missing transverse momentum, $\not{p}_T$. Since the neutrinos escape undetected, the final state invariant mass cannot be reconstructed, and the only distribution sensitive to nonstandard $Z\gamma V$ couplings is the photon p_T spectrum. Compared to the charged lepton decay mode of the Z boson, the decay $Z\to\bar{\nu}\nu$ offers potential advantages. Because of the larger $Z\to\bar{\nu}\nu$ branching ratio, the differential cross section is about a factor 3 larger than that for $q\bar{q}\to e^+e^-\gamma$ and $q\bar{q}\to\mu^+\mu^-\gamma$ combined. Furthermore, final-state bremsstrahlung and timelike virtual photon diagrams do not contribute for the $\bar{\nu}\nu\gamma$ final state. On the other hand, there are several potentially serious background processes which contribute to $p\bar{p}\to\gamma\not{p}_T$, but not to the $l^+l^-\gamma$ final state.

The two most important background processes are prompt photon production, $p\bar{p}\to\gamma j$, with the jet rapidity outside the range covered by the detector and thus "faking" missing transverse momentum, and two jet production where one of the jets is misidentified as a photon while the other disappears through the beam hole. For a realistic assessment of both backgrounds, a full-fledged Monte Carlo simulation is required. Here, for a first rough estimate, we use a simple parton level calculation. For a jet, i.e., a quark or gluon, to be misidentified as $\not{p}_T$ at the Tevatron, we shall require that the jet pseudorapidity be $|\eta_j|>4$. The CDF hadron calorimeter, for example, covers the region $|\eta|<4.2$ [24]. QCD jets typically have a "width" of $\Delta\eta=0.25$ at the Tevatron [24], and thus contribute significantly to the $\not{p}_T$ in an event for $|\eta|>4$. For the probability $P_{\gamma/j}$ that a jet fakes a photon, we shall use Eqs. (3.6) and (3.7).

Our results for signal and backgrounds are summarized in Fig. 11 for $p_{T\gamma}>10$ GeV and a cut on the photon rapidity of $|\eta_\gamma|<3$. The solid line displays the SM prediction for $d\sigma/dp_{T\gamma}$. The dashed (dotted) curve shows the expectation for an anomalous $ZZ\gamma$ coupling $h_{30}^Z=1$ ($h_{40}^Z=0.05$) with $\Lambda=0.75$ TeV. As in Fig. 10, only one coupling at a time is chosen different from its zero SM value. One observes that the γj (dash dotted line) and jj (long dashed line) backgrounds are both much larger than the $\gamma\not{p}_T$ signal at small photon transverse momentum. Because of kinematical constraints, however, they drop rapidly with p_T. In a more complete treatment in which soft gluon and/or quark radiation and hadronization effects are included, one expects that the photon p_T distribution will be somewhat harder for the background processes, especially at high transverse momenta. It is interesting to note that, although $P_{\gamma/j}$ is typically a few $\times10^{-3}$ in the low p_T range, the jj background is larger than that originating from prompt photon production. The relatively larger 2 jet production rate is due primarily to the larger QCD coupling constant, and the much larger number of subprocesses which contribute to jj production. The dot-dot dashed line, finally, shows the background from $p\bar{p}\to Zj$ with the jet misidentified as a photon in the region where Eq. (3.6) is meaningful. This background does not pose a serious problem.

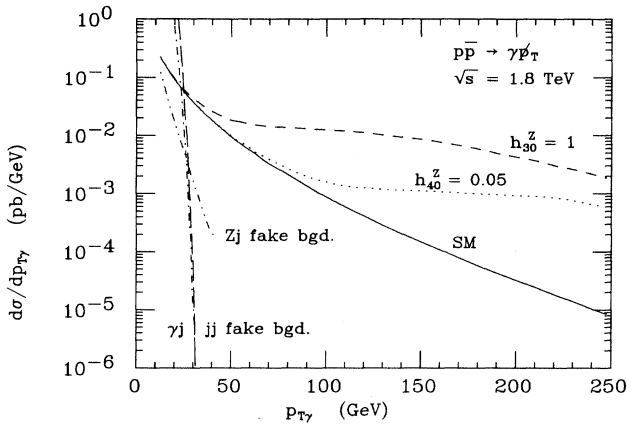

FIG. 11. Transverse momentum distribution of the photon in $p\bar{p}\to\gamma\not{p}_T$ at the Tevatron. The solid line gives the SM prediction. The dashed (dotted) curve shows $d\sigma/dp_{T\gamma}$ for an anomalous $ZZ\gamma$ coupling $h_{30}^Z=1$ ($h_{40}^Z=0.05$) with $\Lambda=0.75$ TeV. Background cross sections are indicated by the long dashed (jj), dash dotted (γj), and dot-dot dashed (Zj) curves. The photon is required to have $p_{T\gamma}>10$ GeV and $|\eta_\gamma|<3$.

Our simulation of the γj and jj backgrounds in $p\bar{p}\to\gamma\not{p}_T$ suggests that those backgrounds can be eliminated effectively by requiring a sufficiently large transverse momentum for the photon. The exact value can be determined only from a full Monte Carlo study. The parton level simulation we performed suggests that $p_{T\gamma}>30$ GeV will be sufficient. Since nonstandard $ZZ\gamma$ and $Z\gamma\gamma$ couplings lead to large deviations from the SM only in the region $p_{T\gamma}>40$ GeV (see Fig. 11), essentially no sensitivity is lost by imposing a $p_{T\gamma}>30$ GeV cut.

D. Sensitivity limits from Tevatron experiments

As we have demonstrated so far, the $m_{ll\gamma}$, $p_{T\gamma}$, and $d\sigma/d\cos\Theta_l^*$ distributions are sensitive indicators of anomalous couplings. We now want to make this statement more quantitative by deriving those values of h_{i0}^V, $V=\gamma,Z$, which would give rise to a deviation from the SM at the level of one or two standard deviations (68% or 95% confidence level) in $d\sigma/dm_{ll\gamma}$ for $p\bar{p}\to l^+l^-\gamma$, and in $d\sigma/dp_{T\gamma}$ for $p\bar{p}\to\gamma\not{p}_T$. We have chosen the invariant mass distribution for the charged lepton final

state since its shape is less sensitive to higher-order QCD corrections than the photon p_T distribution [21]. The shape of the angular distribution of the final-state charged leptons depends too strongly on the cuts imposed in order to be useful for the extraction of sensitivity limits. We assume an integrated luminosity of $\int \mathcal{L}\, dt = 100$ pb^{-1} at the Tevatron, and the following set of cuts for the $l^+l^-\gamma$ final state:

$$\begin{aligned} &m_{ll\gamma} > 100 \text{ GeV}, \quad m_{ll} > 50 \text{ GeV} , \\ &p_{T\gamma} > 10 \text{ GeV}, \quad |\eta_\gamma| < 3 , \\ &p_{Tl} > 15 \text{ GeV}, \quad |\eta_l| < 3.5 , \\ &\Delta R_{l\gamma} > 0.7 . \end{aligned} \tag{3.8}$$

In $p\bar{p} \to \gamma \not{p}_T$ we require

$$p_{T\gamma} > 30 \text{ GeV}, \quad |\eta_\gamma| < 3 . \tag{3.9}$$

Within these cuts one expects about 90 $l^+l^-\gamma$ and 60 $\gamma \not{p}_T$ SM events for 100 pb^{-1}.

The statistical significance is calculated by splitting the $m_{ll\gamma}$ and $p_{T\gamma}$ distributions into five bins, each with more than five events typically. In each bin the Poisson statistics is approximated by a Gaussian distribution. In order to achieve a sizable counting rate in each bin, all events with $m_{ll\gamma} > 220$ GeV and $p_{T\gamma} > 70$ GeV are collected into a single bin. In our calculation, this procedure guarantees that a high statistical significance cannot arise from a single event at high $m_{ll\gamma}$ or $p_{T\gamma}$ where the SM predicts, for example, only 0.01 events. In order to derive realistic limits we allow for a normalization uncertainty $\Delta\mathcal{N}$ of the SM cross section of $\Delta\mathcal{N} = 50\%$. The cuts summarized in Eqs. (3.8) and (3.9) select a phase-space region where backgrounds are small (see Secs. III B and III C). Background contributions are therefore not included in our derivation of sensitivity limits. The expression for χ^2 which is then used to compute confidence levels is given by

$$\chi^2 = \sum_{i=1}^{n_D} \frac{(N_i - f N_i^0)^2}{f N_i^0} + (n_D - 1) , \tag{3.10}$$

where n_D is the number of bins, N_i is the number of events for anomalous couplings, and N_i^0 is the number of events in the SM, in the ith bin. f reflects the uncertainty in the normalization of the SM cross section within the allowed range, and is determined by minimizing χ^2:

$$f = \begin{cases} (1+\Delta\mathcal{N})^{-1} & \text{for } \bar{f} < (1+\Delta\mathcal{N})^{-1} \\ \bar{f} & \text{for } (1+\Delta\mathcal{N})^{-1} < \bar{f} < 1+\Delta\mathcal{N} \\ 1+\Delta\mathcal{N} & \text{for } \bar{f} > 1+\Delta\mathcal{N} \end{cases} \tag{3.11}$$

with

$$\bar{f}^2 = \left[\sum_{i=1}^{n_D} N_i^0 \right]^{-1} \sum_{i=1}^{n_D} \frac{N_i^2}{N_i^0} . \tag{3.12}$$

The calculation of sensitivity bounds is facilitated by the observation that the *CP*-conserving couplings $h_{3,4}^V$ and the *CP*-violating couplings $h_{1,2}^V$ do not interfere. Furthermore, cross sections and sensitivities are nearly identical for equal values of $h_{10,20}^V$ and $h_{30,40}^V$. In the following we shall therefore concentrate on $h_{3,4}^V$. It turns out that $ZZ\gamma$ and $Z\gamma\gamma$ couplings interfere only very little with each other. This result is demonstrated in Fig. 12, where we show the 1σ (dashed lines) and 2σ (solid lines) limit contours, obtained using the procedure outlined above, for $p\bar{p} \to l^+l^-\gamma$ and all possible combinations of $h_{30,40}^Z$ vs $h_{30,40}^\gamma$. Here we used our standard set of form-factor parameters, $n = 3$ for h_3^V and $n = 4$ for h_4^V, and a cutoff scale of $\Lambda = 0.5$ TeV. In each graph, only those couplings plotted against each other are assumed to be different from their zero SM values. The contour lines show that interference effects are small; the extrema of the 1σ and 2σ curves are always quite close to those

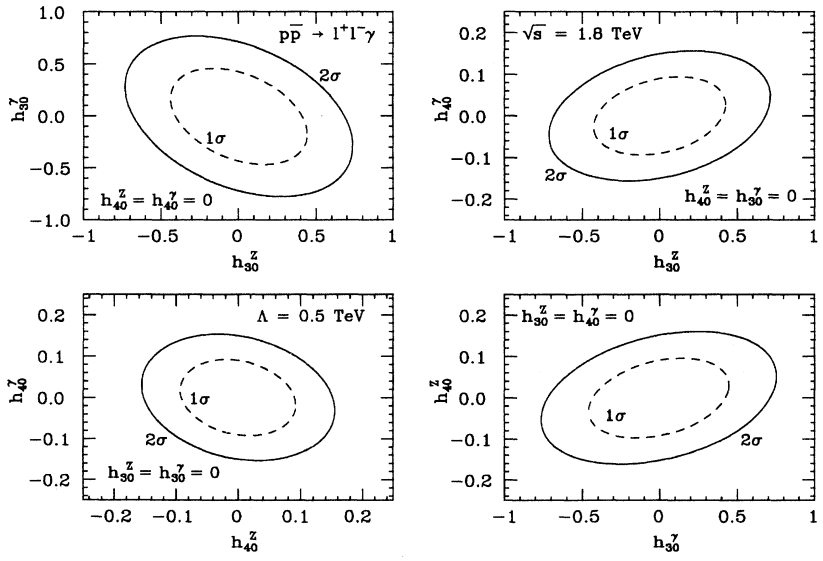

FIG. 12. Shown are the 1σ (dashed lines) and 2σ (solid lines) limit contours of all combinations of $h_{30,40}^Z$ vs $h_{30,40}^\gamma$ derived from the $m_{ll\gamma}$ distribution in $p\bar{p} \to l^+l^-\gamma$ at the Tevatron. An integrated luminosity of 100 pb^{-1} and a form-factor scale of $\Lambda = 0.5$ TeV have been assumed. In each graph, only those couplings which are plotted against each other are assumed to be different from their zero SM values.

values obtained by setting one of the varied couplings equal to zero. For example, for h_{30}^Z vs h_{30}^γ (top left plot), the 2σ limits are $h_{30}^\gamma = \pm 0.77$ for arbitrary values of h_{30}^Z, whereas $h_{30}^\gamma = \pm 0.72$ for $h_{30}^Z = 0$. Plots similar to those shown in Fig. 12 can be obtained for different values of Λ, as well as for $p\bar{p} \to \gamma \not{p}_T$.

Non-negligible interference effects are found between h_3^V and h_4^V, $V = Z, \gamma$. As a result, different anomalous contributions to the helicity amplitudes may cancel partially, resulting in weaker bounds than if only one coupling at a time is allowed to deviate from its SM value. The 1σ and 2σ limit contours for h_{30}^V and h_{40}^V from $p\bar{p} \to l^+ l^- \gamma$ and $p\bar{p} \to \gamma \not{p}_T$ are shown in Figs. 13 and 14. Sensitivity limits are displayed for two values of the form-factor scale, $\Lambda = 0.5$ and 1 TeV. Since interference effects between $ZZ\gamma$ and $Z\gamma\gamma$ couplings are small, we have assumed that $h_3^\gamma = h_4^\gamma = 0$ in Fig. 13. Similarly, we have taken $h_3^Z = h_4^Z = 0$ in Fig. 14. Several observations can be made from the two figures.

(1) The limits found for $Z\gamma\gamma$ couplings are about 3–5% weaker than those for the corresponding $ZZ\gamma$ coupling.

(2) The bounds obtained from $p\bar{p} \to \gamma \not{p}_T$ are approximately a factor 1.5 better than those from $p\bar{p} \to l^+ l^- \gamma$.

(3) The sensitivity limits depend significantly on the form-factor scale Λ. In Table I we list the 1σ and 2σ limits for h_3^Z and h_4^Z from $p\bar{p} \to \gamma \not{p}_T$ at the Tevatron. The bounds on $h_{30}^Z (h_{40}^Z)$ improve by about a factor 3 (6) if Λ is increased from 0.5 to 1 TeV.

(4) The limits depend only marginally on the sign of the various anomalous couplings (see Table I).

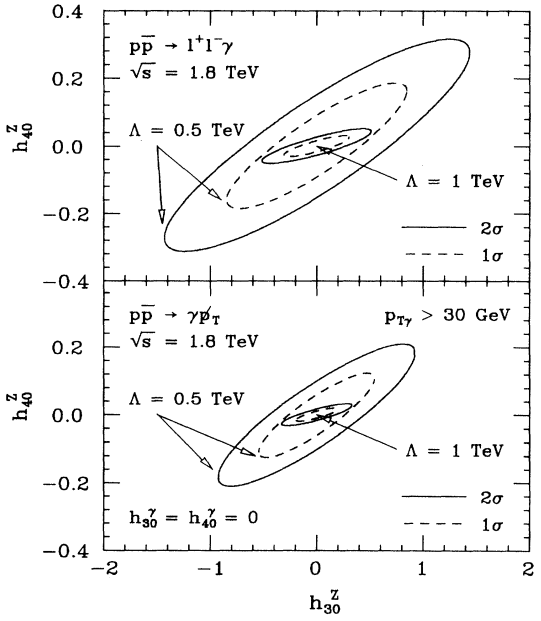

FIG. 13. Shown are the 1σ (dashed lines) and 2σ (solid lines) limit contours for h_{30}^Z vs h_{40}^Z from $p\bar{p} \to l^+ l^- \gamma$ and $p\bar{p} \to \gamma \not{p}_T$ at the Tevatron. The sensitivity bounds are displayed for an integrated luminosity of 100 pb^{-1} and two choices of the form-factor cutoff scale: $\Lambda = 0.5$ and 1 TeV. The two other couplings h_{30}^γ and h_{40}^γ are assumed to be zero.

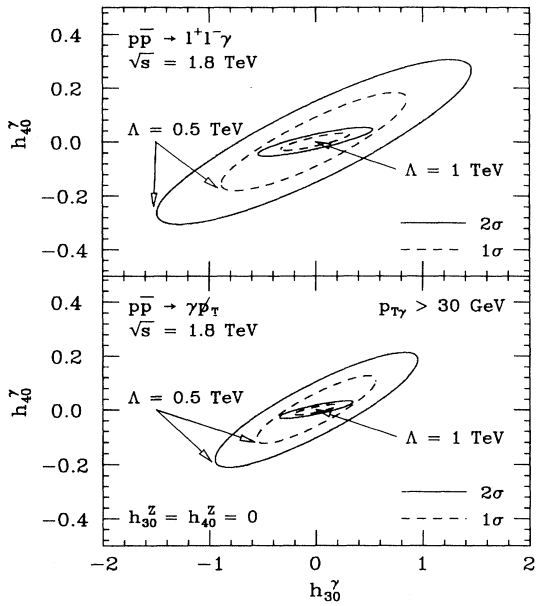

FIG. 14. Shown are the 1σ (dashed lines) and 2σ (solid lines) limit contours for h_{30}^γ vs h_{40}^γ from $p\bar{p} \to l^+ l^- \gamma$ and $p\bar{p} \to \gamma \not{p}_T$ at the Tevatron. The sensitivity bounds are displayed for an integrated luminosity of 100 pb^{-1} and two choices of the form-factor cutoff scale: $\Lambda = 0.5$ and 1 TeV. The two other couplings h_{30}^Z and h_{40}^Z are assumed to be zero.

The dependence of the limits on the cutoff scale Λ in the form factor can be understood easily from Fig. 10(b). The improvement in sensitivity with increasing Λ is due to the additional events at large $m_{ll\gamma}$ or $p_{T\gamma}$ which are suppressed by the form factor if the scale Λ has a smaller value. To a lesser degree, the bounds also depend on the power n in the form factor. In Figs. 13 and 14, and also in Table I, we have taken $n = 3$ for h_3^V and $n = 4$ for h_4^V. For this choice, the high-energy behavior of terms proportional to h_3^V and h_4^V in the amplitudes is the same, thus maximizing interference effects. Had we instead chosen the same power n for both h_3^V and h_4^V, the

TABLE I. Sensitivities achievable at the 1σ and 2σ confidence levels (C.L.) for the anomalous $ZZ\gamma$ couplings h_{30}^Z and h_{40}^Z in $p\bar{p} \to \gamma \not{p}_T$ at the Tevatron for an integrated luminosity of 100 pb^{-1}. The limits for h_{30}^Z apply for arbitrary values of h_{40}^Z, and vice versa. For the form factors we use Eq. (2.8) with $n = 3$ and 4 for h_{30}^Z and h_{40}^Z, respectively. Anomalous $Z\gamma\gamma$ couplings are assumed to be zero.

Coupling	C.L.	$\Lambda = 0.5$ TeV	$\Lambda = 1$ TeV
h_{30}^Z	2σ	$+0.92$ -0.93	$+0.33$ -0.33
	1σ	$+0.54$ -0.55	$+0.20$ -0.20
h_{40}^Z	2σ	$+0.21$ -0.21	$+0.033$ -0.032
	1σ	$+0.12$ -0.12	$+0.020$ -0.020

different high-energy behavior of the amplitudes would have prevented large cancellations between different anomalous contributions.

Equations (2.9) and (2.10) show that unitarity forces the low-energy values of the form factors to decrease quickly with increasing Λ, and, finally, to become so small that no deviation from the SM will be observable in hadron collider experiments. The maximum scale one can probe at the 95% confidence level (C.L.) with $h^V_{1,3}$ at the Tevatron turns out to be $\Lambda \approx 2.1$ TeV for the form factor (2.8) with $n=3$ and an integrated luminosity of 100 pb^{-1}. The corresponding maximal value for $h^V_{2,4}$ is $\Lambda \approx 1.2$ TeV with $n=4$.

The sensitivity to anomalous couplings in $q\bar{q} \to Z\gamma$ stems from regions of phase space where the anomalous contributions to the cross section are considerably larger than the SM expectation. As a result, interference effects between the SM amplitude and the anomalous contributions play a minor role, and the limits are almost independent of the sign of the couplings. Another important consequence is that bounds scale essentially like $(\int \mathcal{L}\, dt)^{1/4}$. Therefore, increasing the integrated luminosity at the Tevatron to 10^3 pb^{-1}, as foreseen by the end of the decade, will improve sensitivity limits of Figs. 13 and 14 by only about a factor 1.8. Similarly, finite experimental lepton detection efficiencies are not expected to significantly weaken those limits.

While a detailed analysis of $Z\gamma$ production at the Tevatron requires a minimum integrated luminosity of the order of 100 pb^{-1}, a few $l^+l^-\gamma$ events may already be found in the available data set. For $\int \mathcal{L}\, dt = 4.7$ pb^{-1} one expects approximately four events within the cuts summarized in (3.8). Since the expected number of $l^+l^-\gamma$ events is very small, the only meaningful observable which can be used to derive bounds on anomalous couplings from present Tevatron data is the total cross section within cuts. Assuming that the cross section can be determined within 50%, the 95% C.L. bounds ($V=\gamma,Z$)

$$\begin{aligned} h^V_{10,30} &= \pm 3.8\ (\pm 2.4)\ , \\ h_{20,40} &= \pm 0.65\ (\pm 0.24) \end{aligned} \tag{3.13}$$

can be reached for $\Lambda = 0.5$ TeV (1 TeV). The limits for $\Lambda = 1$ TeV are already above those allowed by unitarity. The present data sample is sensitive to a scale of about 900 GeV (700 GeV) for $h^V_{1,3}$ ($h^V_{2,4}$).

The sensitivity bounds shown in Figs. 12–14 and Table I were derived without taking into account the change in the shape of $d\sigma/dm_{ll\gamma}$ and $d\sigma/dp_{T\gamma}$ resulting from higher-order QCD corrections [21]. QCD corrections were found to change the shape of the $Z\gamma$ invariant mass distribution only very mildly at Tevatron energies, resulting in an increase of the differential cross section of about a factor 1.25 at $m_{Z\gamma}=100$ GeV, and a factor 1.3 at $m_{Z\gamma}=500$ GeV. The sensitivity limits derived from $m_{ll\gamma}$ are therefore not expected to change substantially if QCD corrections are included in the analysis. The bounds obtained from the photon transverse momentum distribution, on the other hand, may be somewhat more sensitive to QCD corrections. Once next-to-leading-log QCD corrections are taken into account, the $Z\gamma$ system can have a nonzero transverse momentum. The shape of the $p_{T\gamma}$ distribution is therefore affected more by higher-order QCD effects than $d\sigma/dm_{Z\gamma}$. For $p_{T\gamma}=30$ GeV the differential cross section increases by about a factor 1.2, and by a factor 1.4 at a photon transverse momentum of 200 GeV [21]. In order to take QCD corrections into account consistently in the derivation of sensitivity limits, they must be known for arbitrary $ZZ\gamma$ and $Z\gamma\gamma$ couplings. The calculation presently available is valid only for SM couplings.

IV. SIGNALS OF ANOMALOUS $ZZ\gamma$ AND $Z\gamma\gamma$ COUPLINGS AT THE LHC AND SSC

In Sec. III we presented a detailed analysis of the signatures of anomalous $ZZ\gamma$ and $Z\gamma\gamma$ couplings at the Tevatron. We now repeat the most important steps of this analysis for the planned hadron supercolliders LHC (pp collisions at $\sqrt{s}=15.4$ TeV [25]) and SSC (pp collisions at $\sqrt{s}=40$ TeV). To simulate detector response, we shall impose the following set of cuts:

$$\begin{aligned} &p_{T\gamma} > 100 \text{ GeV}, \quad |\eta_\gamma| < 3\ , \\ &p_{Tl} > 20 \text{ GeV}, \quad |\eta_l| < 3\ , \\ &m_{ll} > 50 \text{ GeV}, \quad \Delta R_{l\gamma} > 0.7\ . \end{aligned} \tag{4.1}$$

The large photon transverse momentum cut automatically selects a region of phase space in which $Z\gamma$ production dominates. Moreover, in this region the photon jet misidentification probability is small [26,27]. Energy mismeasurements in the detector are simulated by Gaussian smearing of the charged lepton and photon momenta with standard deviation

$$\frac{\sigma}{E} = \begin{cases} 0.14/\sqrt{E_T} \oplus 0.01 & \text{for } |\eta| < 1.4 \\ 0.17/\sqrt{E_L} \oplus 0.01 & \text{for } 1.4 < |\eta| < 3 \\ 0.5/\sqrt{E_L} \oplus 0.05 & \text{for } 3 < |\eta| < 5 \end{cases} \tag{4.2}$$

corresponding to the energy resolution foreseen for the Solenoidal Detector Collaboration (SDC) [28]. Here E_T (E_L) is the transverse (longitudinal) component of the energy E, and the symbol $\oplus$ signifies that the constant term is added in quadrature in the resolution.

Owing to the extremely large gluon luminosity, one expects that gluon fusion, $gg \to Z\gamma$, contributes more significantly at the LHC and SSC than the Tevatron energies. For the photon transverse momentum and rapidity cut of (4.1) one finds that the $gg \to Z\gamma$ cross section is about 6% (14%) of the $q\bar{q} \to Z\gamma$ cross section at the LHC (SSC) [22]. It is thus much smaller than next-to-leading-log QCD corrections, which amount to about 50% of the Born cross section [21]. As in our discussion for the Tevatron, we shall not include NLL QCD effects nor the contribution from gluon fusion in our subsequent analysis.

The signals of anomalous couplings at the LHC and SSC are qualitatively the same as at the Tevatron. One expects a broad enhancement of the cross section at large

values of $m_{ll\gamma}$ and at large photon transverse momenta. The effects of anomalous couplings on the $ll\gamma$ invariant mass distribution at the LHC and SSC are illustrated in Fig. 15 for $h_{30}^Z=0.02$ (dashed line) and $h_{40}^Z=2\times10^{-4}$ (dotted line), and a form-factor cutoff scale of $\Lambda=2$ TeV. Only one coupling at a time is chosen different from its zero SM value. Furthermore, we have summed over electron and muon final states. Figure 15 shows that the large photon transverse momentum cut of $p_{T\gamma}>100$ GeV has no appreciable effect on the observability of anomalous $ZZ\gamma$ and $Z\gamma\gamma$ couplings. The LHC and SSC will be sensitive to much smaller values of anomalous couplings than the Tevatron. Taking into account the form-factor behavior will be absolutely essential at hadron supercolliders, even for small anomalous couplings.

If the photon jet misidentification probability $P_{\gamma/j}$ is $\sim10^{-4}$, or smaller for $p_{T\gamma}>100$ GeV, as suggested by present studies [26,27], the background from l^+l^-j production is small. Backgrounds arising from jets misidentified as isolated electrons should be even smaller [27]. For $pp\to\gamma\not{p}_T$, prompt photon and 2 jet production are expected to be a problem at small photon transverse momenta. If the region out to $|\eta|=5$ is covered by the hadron calorimeter [28], a parton level study suggests that a cut of $p_{T\gamma}>200$ GeV is sufficient to eliminate the γj and jj background.

Sensitivity bounds can be calculated for anomalous $ZZ\gamma$ and $Z\gamma\gamma$ couplings at the LHC or SSC based on a procedure analogous to that in Sec. III D. We illustrate the sensitivities achievable at hadron supercolliders in Fig. 16 where we plot the 1σ (dashed lines) and 2σ (solid lines) limit contours for h_{30}^Z vs h_{40}^Z obtained from the invariant mass distribution in $pp\to l^+l^-\gamma$, imposing the cuts summarized in Eq. (4.1). The $m_{ll\gamma}$ distribution is split into 7 (8) bins at the LHC (SSC). To achieve a sufficient number of events in each bin, all events with $m_{ll\gamma}>1.4$ TeV (1.7 TeV) are combined in a single bin. We assume an integrated cross section of $\int\mathcal{L}\,dt=10^4$ pb^{-1} for both LHC and SSC, and allow for a normalization uncertainty $\Delta\mathcal{N}$ of the SM cross section of $\Delta N=50\%$. Contours are shown for $\Lambda=2$ and 3 TeV. For convenience, the 1σ and 2σ limits are also collected in Table II.

For equal integrated luminosities, the sensitivities which can be reached at the SSC are a factor 1.5–3 better than those achievable at the LHC. Comparison with Figs. 13 and 14 shows that hadron supercolliders can improve the measurement of the $ZZ\gamma$ and $Z\gamma\gamma$ vertices by up to three orders of magnitude beyond that expected from Tevatron experiments. In spite of the high sensitivity to the anomalous couplings h_i^V, $V=\gamma,Z$, neither the LHC nor the SSC will be able to test the radiative corrections to these quantities in the SM, which are at best of $\sim10^{-4}$ [see Eq. (2.4)]. In the SM, the form factors vary on a scale given by the masses of particles in the loop dia-

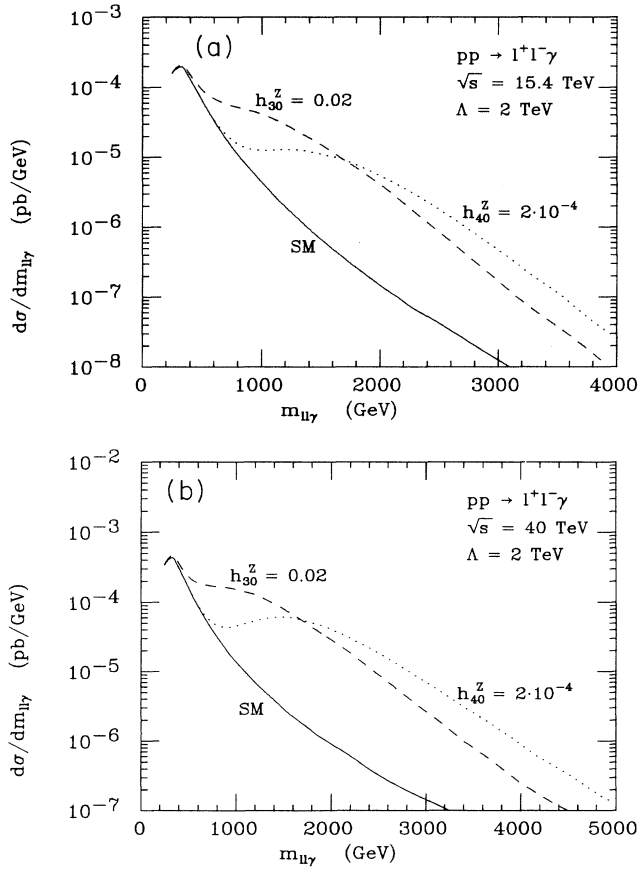

FIG. 15. The distribution $d\sigma/dm_{ll\gamma}$ at (a) the LHC and (b) the SSC. The curves are for the SM (solid curve), $h_{30}^Z=0.02$ (dashed line), and $h_{40}^Z=2\times10^{-4}$ (dotted line). For the form factor we have chosen Eq. (2.8) with $\Lambda=2$ TeV, and $n=3$ ($n=4$) for h_3^Z (h_4^Z). Cuts are specified in Eq. (4.1).

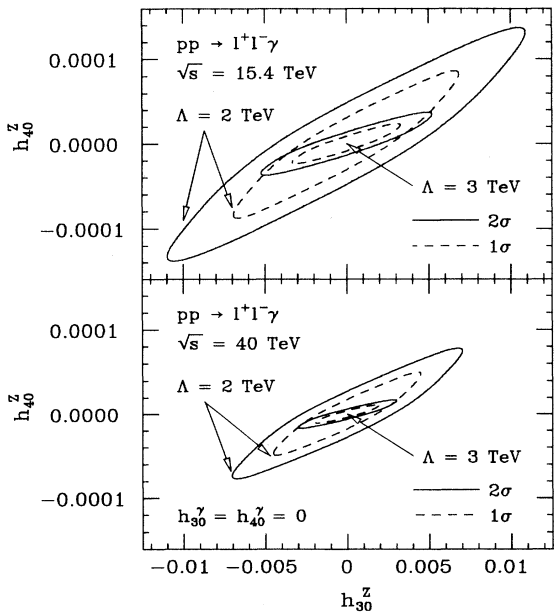

FIG. 16. Shown are the 1σ (dashed lines) and 2σ (solid lines) limit contours for h_{30}^Z vs h_{40}^Z from $pp\to l^+l^-\gamma$ at the LHC and SSC. The sensitivity bounds are displayed for an integrated luminosity of 10^4 pb^{-1} and two choices of the form-factor cutoff scale: $\Lambda=2$ and 3 TeV. The two other couplings h_{30}^γ and h_{40}^γ are assumed to be zero.

TABLE II. Sensitivities achievable at the 1σ and 2σ confidence levels (C.L.) for the anomalous $ZZ\gamma$ couplings h_{30}^Z and h_{40}^Z in $pp \to l^+l^-\gamma$ at the LHC and SSC for an integrated luminosity of 10^4 pb^{-1}. The limits for h_{30}^Z apply for arbitrary values of h_{40}^Z, and vice versa. For the form factors we use Eq. (2.8) with $n=3$ and 4 for h_{30}^Z and h_{40}^Z, respectively. Anomalous $Z\gamma\gamma$ couplings are assumed to be zero. (a) LHC bounds, $\sqrt{s}=15.4$ TeV. (b) SSC bounds, $\sqrt{s}=40$ TeV.

Coupling	C.L.	$\Lambda=2$ TeV	$\Lambda=3$ TeV
		(a)	
h_{30}^Z	2σ	$+1.1\times10^{-2}$	$+5.2\times10^{-3}$
		-1.1×10^{-2}	-5.2×10^{-3}
	1σ	$+6.8\times10^{-3}$	$+3.3\times10^{-3}$
		-6.9×10^{-3}	-3.3×10^{-3}
h_{40}^Z	2σ	$+1.4\times10^{-4}$	$+3.7\times10^{-5}$
		-1.4×10^{-4}	-3.7×10^{-5}
	1σ	$+8.6\times10^{-5}$	$+2.4\times10^{-5}$
		-8.8×10^{-5}	-2.4×10^{-5}
		(b)	
h_{30}^Z	2σ	$+7.0\times10^{-3}$	$+3.0\times10^{-3}$
		-7.0×10^{-3}	-3.0×10^{-3}
	1σ	$+4.5\times10^{-3}$	$+1.9\times10^{-3}$
		-4.5×10^{-3}	-1.9×10^{-3}
h_{40}^Z	2σ	$+7.8\times10^{-5}$	$+1.7\times10^{-5}$
		-7.7×10^{-5}	-1.7×10^{-5}
	1σ	$+5.0\times10^{-5}$	$+1.1\times10^{-5}$
		-4.9×10^{-5}	-1.1×10^{-5}

grams, e.g., the weak-boson masses or the top-quark mass. These are in the few hundred GeV range, and according to Table II, future pp colliders are not able to limit anomalous $ZZ\gamma$ and $Z\gamma\gamma$ couplings to better than $\sim 10^{-2}$ for scales in this range.

The much larger energies available at the LHC and SSC also mean that higher scales Λ can be probed. Saturating the unitarity limits and using the form factor (2.8), we find that the maximum scale accessible (95% C.L.) for $h_{1,3}^V$ with $n=3$ at the LHC (SSC) is about 11 TeV (18 TeV), and approximately 6 TeV (10 TeV) for $h_{2,4}^V$ with $n=4$. Z photon production at hadron supercolliders thus provides a tool to investigate the properties of the weak-boson sector well above the few TeV region where the production of new particles may yield a more direct signature.

We have not considered in detail the sensitivities achievable in $pp \to \gamma \not{p}_T$ at supercollider energies. If this reaction can be utilized, it should yield limits slightly better than those derived from $pp \to l^+l^-\gamma$, due to the larger $Z \to \bar{\nu}\nu$ branching ratio. The limits shown in Fig. 16 and Table II do not incorporate the effects of NLL QCD corrections. These corrections are much more significant at LHC and SSC energies than at the Tevatron [21]. Our sensitivity bounds should be regarded therefore only as illustrations of the capabilities of future hadron supercolliders.

V. DISCUSSION AND CONCLUSIONS

In Secs. III and IV we described the signatures that anomalies in the $ZZ\gamma$ and $Z\gamma\gamma$ vertex would produce in $q\bar{q} \to l^+l^-\gamma$, $l=e,\mu$, and $q\bar{q} \to \gamma \not{p}_T$ at the Tevatron, the LHC, and the SSC. The $l^+l^-\gamma$ invariant mass spectrum, the photon transverse momentum and the $\cos\Theta_l^*$ distributions were found to be sensitive indicators of anomalous couplings. In addition, we determined how large deviations from the SM must be in order to yield visible effects. Our analysis improves on the existing literature [4,5] in that we include the full set of anomalous couplings allowed by Lorentz and electromagnetic gauge invariance. We also take into account the form-factor effects of the nonstandard $ZZ\gamma$ and $Z\gamma\gamma$ couplings. Furthermore, we use the full set of tree level Feynman diagrams, including timelike virtual photon and final-state bremsstrahlung diagrams, and derive realistic sensitivity limits.

It is interesting to compare the sensitivity of hadron collider experiments with existing low-energy limits on anomalous couplings and with the sensitivity to nongauge theory $ZZ\gamma$ and $Z\gamma\gamma$ vertices accessible in e^+e^- collisions. In contrast with the direct measurement of trilinear gauge boson couplings in collider experiments, low-energy bounds on nonstandard trilinear vector boson couplings are model dependent and controversial at present [29–31]. In particular, constraints from quantities which naively depend quadratically, or on a higher power, on the cutoff scale that regularizes the loop divergencies seem to be very sensitive to assumptions about the symmetries of the underlying model and their realization. Limits based on quantities that depend only logarithmically on the cutoff scale such as the anomalous magnetic moment of the muon $(g-2)_\mu$, on the other hand, appear to be more robust and less sensitive to details, and thus are more reliable. Bounds on anomalous $ZZ\gamma$ and $Z\gamma\gamma$ couplings from $(g-2)_\mu$ have been considered in Ref. [32]. It turns out that only $Z\gamma\gamma$ couplings give a nonzero contribution. From present $(g-2)_\mu$ data one obtains, for $h_4^\gamma=0$,

$$\left| h_3^\gamma \ln\left[\frac{\Lambda^2}{m_Z^2}\right] \right| < 9 , \tag{5.1}$$

where Λ is the loop cutoff scale. Limits which can be obtained from the present CDF data set are already competitive with the bound shown in (5.1) [see Eq. (3.13)]. It will be possible to improve this limit significantly with the data sample expected from the new round of experiments. The situation is less clear for the CP-violating couplings $h_{1,2}^V$. It is conceivable that contributions to the electric dipole moment of the neutron yield extremely strong limits on $h_{1,2}^V$, similar to the bounds obtained for the CP-violating $WW\gamma$ couplings $\tilde{\kappa}$ and $\tilde{\lambda}$ [33]. So far, these contributions have not been calculated.

Experiments at the CERN e^+e^- collider LEP and the SLAC Linear Collider (SLC) are also able to probe anomalous $ZZ\gamma$ and $Z\gamma\gamma$ interactions via radiative Z decays:

$$Z \to l^+l^-\gamma \quad \text{and} \quad Z \to \bar{\nu}\nu\gamma . \tag{5.2}$$

The limit on non-SM contributions to the $Z \to e^+e^-\gamma$ branching ratio from LEP data is [34]

$$B(Z \to e^+e^-\gamma) < 5.2\times10^{-4} . \tag{5.3}$$

Similar limits are also obtained for $Z\to\mu^+\mu^-\gamma$ and $Z\to\tau^+\tau^-\gamma$ [34]. In Fig. 4 we see that even large anomalous couplings contribute only at the 1% level to the cross section around the Z peak in $p\bar{p}\to l^+l^-\gamma$. It is therefore not surprising that the upper bound (5.3) translates into rather poor limits on h_i^V. Assuming that only one anomalous coupling is non-zero at a time, we obtain

$$|h^Z_{10,30}|<23,\quad |h^\gamma_{10,30}|<14\ ,$$
$$|h^Z_{20,40}|<62,\quad |h^\gamma_{20,40}|<99\ . \tag{5.4}$$

at 95% C.L. Somewhat better limits can be obtained from $Z\to\bar{\nu}\nu\gamma$ for the $ZZ\gamma$ couplings. From the measured $e^+e^-\to\bar{\nu}\nu\gamma$ cross section [35] at the Z peak we find the 95% C.L. bounds

$$|h^Z_{10,30}|<5\ \text{ and }\ |h^Z_{20,40}|<13\ , \tag{5.5}$$

where we have again varied only one coupling at a time. Much higher sensitivities are expected from LEP II or an e^+e^- collider with $\sqrt{s}=500$ GeV [Next Linear Collider (NLC)]. Studies have found [36–38]

$$|h^Z_3|<\begin{cases}0.3 & \text{at LEP II}\\ 0.01 & \text{at NLC}\end{cases} \tag{5.6}$$

at 95% C.L. Integrated luminosities of 500 pb^{-1} for LEP II, and 10^4 pb^{-1} for the NLC were assumed.

The Tevatron will be able to provide limits on anomalous $ZZ\gamma$ and $Z\gamma\gamma$ couplings which are comparable to those expected from LEP II. Similarly, bounds from the NLC and the LHC or SSC will be competitive if the form factor scale Λ is in the few TeV region. For larger values of Λ the higher energy of the hadron colliders provides a clear advantage over an e^+e^- collider with $\sqrt{s}=500$ GeV. In view of our present poor knowledge of the potential self-interactions of Z bosons and photons, the direct measurement of the $Z\gamma V$ couplings h_i^V via $p\bar{p}\to l^+l^-\gamma$ and $p\bar{p}\to\gamma\not{p}_T$ at the Tevatron will constitute major progress and represent an important step towards a highly precise test of trilinear vector-boson couplings at the LHC and SSC.

ACKNOWLEDGMENTS

We are very grateful to S. Errede for many stimulating discussions and for providing us with details of the CDF detector and the CDF $p\bar{p}\to Z\gamma$ analysis. We would like to thank J. Bagger, F. Boudjema, J. Elias, D. Errede, S. Godfrey, K. Hagiwara, S. Kuhlmann, D. London, T. Müller, J. Ohnemus, R. D. Peccei, G. Valencia, R. G. Wagner, and D. Zeppenfeld for useful discussions. We also acknowledge the assistance of H. Wahl and J. Womersley in obtaining information about the D0 detector. One of us (U.B.) would like to thank the High Energy Physics Division, Argonne National Laboratory, where part of the work was done, for its warm hospitality. This research was supported in part by the U.S. Department of Energy under Contract Nos. W-31-109-ENG-38 and DE-FG05-87ER40319.

[1] UA2 Collaboration, J. Alitti *et al.*, Phys. Lett. B **277**, 194 (1992).
[2] U. Baur and E. L. Berger, Phys. Rev. D **41**, 1476 (1990).
[3] R. W. Brown, K. O. Mikaelian, and D. Sahdev, Phys. Rev. D **20**, 1164 (1979); K. O. Mikaelian, M. A. Samuel, and D. Sahdev, Phys. Rev. Lett. **43**, 746 (1979); F. Renard, Nucl. Phys. **B196**, 93 (1982); E. Eichten, I. Hinchliffe, K. Lane, and C. Quigg, Rev. Mod. Phys. **56**, 579 (1984); **58**, 1065(E) (1986).
[4] H. Baer, V. Barger, and K. Hagiwara, Phys. Rev. D **30**, 1513 (1984).
[5] Z. Ryzak, Nucl. Phys. **B289**, 301 (1987).
[6] K. Hagiwara *et al.*, Nucl. Phys. **B282**, 253 (1987).
[7] R. Barbieri, H. Harari, and M. Leurer, Phys. Lett. **141B**, 455 (1985).
[8] C. N. Yang, Phys. Rev. **77**, 242 (1950).
[9] A. Barroso, F. Boudjema, J. Cole, and N. Dombey, Z. Phys. C **28**, 149 (1985).
[10] J. M. Cornwall, D. N. Levin, and G. Tiktopoulos, Phys. Rev. Lett. **30**, 1268 (1973); Phys. Rev. D **10**, 1145 (1974); C. H. Llewellyn Smith, Phys. Lett. **46B**, 233 (1973); S. D. Joglekar, Ann. Phys. (N.Y.) **83**, 427 (1974).
[11] U. Baur and D. Zeppenfeld, Phys. Lett. B **201**, 383 (1988).
[12] Particle Data Group, K. Hikasa *et al.*, Phys. Rev. D **45**, S1 (1992).
[13] K. Hagiwara and D. Zeppenfeld, Nucl. Phys. **B274**, 1 (1986).
[14] H. Czyz, K. Kolodziej, and M. Zralek, Z. Phys. C **43**, 97 (1989).
[15] F. A. Berends *et al.*, Phys. Lett. **103B**, 124 (1981); P. Aurenche *et al.*, *ibid.* **140B**, 87 (1984); Nucl. Phys. **B286**, 553 (1987); V. Barger, T. Han, J. Ohnemus, and D. Zeppenfeld, Phys. Lett. B **232**, 371 (1989).
[16] CDF Collaboration, F. Abe *et al.*, Phys. Rev. D **45**, 3921 (1992).
[17] S. Errede (private communication); H. Wahl (private communication).
[18] J. Womersley (private communication).
[19] S. Bethke and S. Catani, in *QCD and High Energy Hadronic Interactions,* Proceedings of the XXVIIth Recontre de Moriond, Les Arcs, France, 1992, edited by J. Tran Thanh Van (Editions Frontieres, Gif-sur-Yvette, 1992), p. 203.
[20] J. F. Owens, Phys. Lett. B **266**, 126 (1991).
[21] J. Ohnemus, Phys. Rev. D **47**, 940 (1993).
[22] V. Constantini, B. de Tollis, and G. Pistoni, Nuovo Cimento A **2**, 733 (1971); E. W. N. Glover and J. J. van der Bij, Phys. Lett. B **206**, 701 (1988).
[23] F. A. Berends and R. Kleiss, Z. Phys. C **27**, 365 (1985).
[24] CDF Collaboration, F. Abe *et al.*, Phys. Rev. D **45**, 2249 (1992).
[25] The LHC Study Group, "Design Study of the Large Hadron Collider," CERN Report No. 91-03, 1991 (unpublished).
[26] Y. Morita, in *Physics of the Superconducting Supercollider, Snowmass, 1986,* Proceedings of the Summer Study, Snowmass, Colorado, 1986, edited by R. Donaldson and J. Marx (Division of Particles and Fields of the APS, New

York, 1987), p. 194.
[27] R. Zhu, Report No. CALT-68-1777 (unpublished); R. Zhu and H. Yamamoto, Report No. CALT-68-1802 (unpublished).
[28] SDC Collaboration, E. L. Berger *et al.*, SDC Technical Design Report, SDC-92-201, 1992 (unpublished).
[29] A. de Rújula, M. B. Gavela, P. Hernandez, and E. Masso, Nucl. Phys. **B384**, 3 (1992).
[30] K. Hagiwara, S. Ishihara, R. Szalapski, and D. Zeppenfeld, Phys. Lett. B **283**, 353 (1992).
[31] C. P. Burgess and D. London, Report No. McGill-92/04 (unpublished); Report No. McGill-92/05 (unpublished); Phys. Rev. Lett. **69**, 3428 (1992).
[32] P. Méry, S. E. Moubarik, M. Perrottet, and F. M. Renard, Z. Phys. C **46**, 229 (1990).
[33] W. J. Marciano and A. Queijeiro, Phys. Rev. D **33**, 3449 (1986); F. Boudjema, K. Hagiwara, C. Hamzaoui, and K. Numata, *ibid.* **43**, 2223 (1991).
[34] OPAL Collaboration, P. Acton *et al.*, Phys. Lett. B **273**, 338 (1991).
[35] OPAL Collaboration, M. Z. Akrawy *et al.*, Z. Phys. C **50**, 373 (1991); L3 Collaboration, B. Adeva *et al.*, Phys. Lett. B **275**, 209 (1992); S. Gentile, in *Proceedings of the XXVIth International Conference on High Energy Physics,* Dallas, Texas, 1992, edited by J. Sanford, AIP Conf. Proc. No. 272 (AIP, New York, 1993); L3 Collaboration, O. Adriani *et al.*, Phys. Lett. B **292**, 463 (1992).
[36] P. Méry, M. Perrottet, and F. M. Renard, Z. Phys. C **38**, 579 (1988).
[37] A. Barroso and L. Bento, Phys. Rev. D **38**, 2742 (1988).
[38] F. Boudjema *et al.*, in *Proceedings of* e^+e^- *Collisions at 500 GeV: The Physics Potential,* edited by P. Zerwas (DESY Report No. 92-123A,B, Hamburg, Germany, 1992), Pt. B, p. 717.